

An experimentally validated model of diffusion charging of arbitrary shaped aerosol particles

Li Li, Ranganathan Gopalakrishnan *

Department of Mechanical Engineering, The University of Memphis, Memphis, TN, USA

ARTICLE INFO

Keywords:

Non-spherical aerosols
Arbitrary shape
Unipolar diffusion charging
Bipolar diffusion charging
Langevin dynamics
Fractal aggregates
Cylindrical nanoparticles

ABSTRACT

Particle shape strongly influences the diffusion charging of aerosol particles exposed to bipolar/unipolar ions and accurate modeling is needed to predict the charge distribution of non-spherical particles. A prior particle-ion collision kernel β_i model including Coulombic and image potential interactions for spherical particles is generalized for arbitrary shapes following a scaling approach that uses a continuum and free molecular particle length scale and Langevin dynamics simulations of non-spherical particle-ion collisions for attractive Coulomb-image potential interactions. This extended β_i model for collisions between unlike charged particle-ion (bipolar charging) and like charged particle-ion (unipolar charging) is validated by comparing against published experimental data of bipolar charge distributions for diverse shapes. Comparison to the bipolar charging data for spherical particles shows good agreement in air, argon, and nitrogen, while also demonstrating high accuracy in predicting charge states up to ± 6 . Comparisons to the data for fractal aggregates reveal that the LD-based β_i model predicts within overall $\pm 30\%$ without any systematic bias. The mean charge on linear chain aggregates and charge fractions on cylindrical particles is found to be in good agreement with the measurements ($\sim \pm 20\%$ overall). The comparison with experimental results supports the use of LD-based diffusion charging models to predict the bipolar and unipolar charge distribution of arbitrary shaped aerosol particles for a wide range of particle size, and gas temperature, pressure. The presented β_i model is valid for perfectly conducting particles and in the absence of external electric fields; these simplifications need to be addressed in future work on particle charging.

1. Introduction

Diffusion charging of aerosol particles (typically, ~ 1 nm to several μ m in size suspended in a gas) is driven by the thermal energy $k_B T_g$ and the electrostatic potential energy $\phi(r)$ of ions; the ion transport is followed by a relatively instantaneous charge transfer reaction to the particle that leaves the particle charge z_p modified: $z_p \rightarrow z_p + z_i$, where $z_i = \pm 1$ is the ion's elementary charge. Although experimental studies have shown that particle shape strongly influences the electric charge acquired by aerosol particles exposed to low energy (~ 0.03 keV) unipolar ions (summarized in Table I-A) and bipolar ions (summarized in Table I-B), an accurate model to predict the charge distribution of particles of arbitrary shape remains elusive (Gopalakrishnan et al., 2013b, 2015). The charging rate of aerosol particles R_i ($\text{m}^{-3}\text{s}^{-1}$) of specified size and shape is calculated as the product of the particle-ion collision kernel/collision rate coefficient/attachment coefficient/ion flux coefficient β_i (m^3s^{-1}), the particle number concentration n_p (m^{-3}) and the ion number

* Corresponding author.

E-mail address: rgplkrsh@memphis.edu (R. Gopalakrishnan).

List of symbols (in order of appearance)

T_g	Background gas temperature
p_g	Background gas pressure
k_B	Boltzmann constant
$k_B T_g$	Ion thermal energy
$\phi(r)$	Ion electrostatic potential energy
z_p	Particle elementary charge (integer)
z_i	Ion elementary charge (integer)
R_i	Charging rate of aerosol particles
β_i	Particle-ion collision kernel/collision rate coefficient/attachment coefficient/ion flux coefficient
n_p	Particle number concentration
n_i	Ion number concentration
N, N_p	Number of primary spheres in an agglomerate/aggregate
d_p	Diameter of spherical/cylindrical aerosol particle or diameter of primary sphere
l_p	Length of a cylindrical or chain-like aerosol particle
$N_o t$	Product of nominal ion concentration and the exposure time of particles to ions in a unipolar ion environment
D_f	Fractal dimension of fractal agglomerates/aggregates
d_{me}	Diameter of sphere with the same electrical mobility as a non-spherical particle, commonly referred to as the (electrical) mobility (equivalent) diameter
Kn_D	Diffusive Knudsen number for particle-ion collision process
R_s	Smoluchowski radius; hydrodynamic radius of a non-spherical aerosol particle
PA	Orientation-averaged projected area of a non-spherical aerosol particle
t_R	Timescale of particle rotation
t_i	Timescale of ion translation
I_1, I_2, I_3	Principal moments of inertia of a non-spherical particle
m_p	Mass of particle
η_c	Continuum enhancement factor
η_f	Free molecular enhancement factor
H	Non-dimensional particle-ion collision kernel
k_f	Fractal pre-factor of fractal agglomerates/aggregates
Ψ_E	Electrostatic potential energy associated with Coulomb potential interactions to thermal energy ratio
Ψ_I	Electrostatic potential energy associated with image potential interactions to thermal energy ratio
ϵ_o	Permittivity of vacuum
e	Electronic charge
ϵ_r	Dielectric constant of particle material
a_p	Radius of spherical/cylindrical particle or radius of primary sphere
f_i	Ion friction factor
μ_i	Ion electrical mobility
D_i	Ion self-diffusion coefficient
r	Non-dimensional separation between the particle and ion
m_i	Ion mass
\vec{v}_i	Ion velocity
t	Time
$[\cdot]_C$	Quantity $[\cdot]$ computed numerically using a suitable technique referenced in the main text
$[\cdot]_{eq.X}$	Quantity $[\cdot]$ analytically computed using eq.X
$[\cdot]_{eq.COMSOL}$	Quantity $[\cdot]$ computed using COMSOL®
$[\cdot]_{LD}$	Quantity $[\cdot]$ computed using Langevin Dynamics (LD)
$n_{i p}$	Ion concentration at the surface of a non-spherical particle
\bar{c}	Ion mean thermal speed
v	Non-dimensional speed of the ion
b_c	Non-dimensional impact parameter of the ion
L_H	Length scale used to normalize the collision kernel β_i
L_{Kn}	Length scale used to calculate Kn_D
$H_{HS}(Kn_D)$	Hard sphere non-dimensional collision kernel H given by eq. 9
μ	Parameter that appears in eq. 10a
A, B, C, k	Fit constants that appear in eq. 10b
p	Particle charge number (integer)

f_p	Fraction of particles carrying p charges
POS	Number of positive ions in an ion population
NEG	Number of negative ions in an ion population
$\beta_{p,i\pm}$	Collision kernel between a particle carrying p charges and the i^{th} type of \pm ion
$\theta_{i\pm}$	Relative abundance of the i^{th} type of \pm ion
$R_{p \rightarrow p \pm 1}$	Total charging rate of a particle carrying p charges moving to a charge state of $p \pm 1$
$n_{T\pm}$	Total concentration of \pm ions
$f_p^{eq.11}$	Charge fraction computed using eq. (11)
f_p^{exp}	Experimentally measured charge fraction
$\langle p \rangle^{eq.11}$	Average charge per particle computed using eq. 11
$\langle p \rangle^{exp}$	Experimentally measured average charge per particle
ζ_p	Particle (scalar) friction factor
Q_{DMA}	DMA Sheath flow rate
V_{DMA}	DMA classification voltage
r_o, r_i	Outer and inner radii of DMA classifier
L	Length of DMA classification region
Z_{DMA}	Centroid mobility corresponding to DMA operating settings
β_i^{NS}	Particle-ion collision kernel for a non-spherical particle
β_i^S	Particle-ion collision kernel for a spherical particle with the same electrical mobility as a non-spherical particle in question
f_p^{NS}	Particle charge fraction for a non-spherical particle
f_p^S	Particle charge fraction for a spherical particle with the same electrical mobility as a non-spherical particle in question
β_i^{CI}	Particle-ion collision kernel including both Coulomb and image potential
β_i^C	Particle-ion collision kernel including only Coulomb potential

concentration n_i (m^{-3}): $R_i = \beta_i n_p n_i$. The inference of the collision kernel β_i for *spherical* aerosol particles has been the subject of numerous theoretical treatments (Bricard, 1962; Fuchs, 1963; Marlow, 1980; Hoppel & Frick, 1986; Lushnikov & Kulmala, 2004; D'Yachkov et al., 2007; Gatti & Kortshagen, 2008; Gopalakrishnan & Hogan, 2012; Ouyang et al., 2012; Gopalakrishnan, Meredith, et al., 2013; Gopalakrishnan, Thajudeen, et al., 2013; Lopez-Yglesias & Flagan, 2013; Chahl & Gopalakrishnan, 2019; Sharma et al., 2019) and experimental investigations (Adachi et al., 1985, 1987, 1989, 1992, 1993; Hussin et al., 1983; Porstendorfer et al., 1979, 1984; Reischl et al., 1983), most recently reviewed by Li et al. (2020) and Johnson et al. (2020). In this article, we focus on the effect of particle shape on β_i , advance a model for the same and compare the predictions of the developed model against published bipolar charging experimental data.

Particle capacitance has been shown to determine the ion flux on to a particle of any shape in the continuum regime of diffusion charging (Chang, 1981; Chang & Laframboise, 1976; Filippov, 1994; Laframboise & Chang, 1977), in which the ion's motion with respect to the particle is diffuse or random. Wen et al. (1984a) used the Boltzmann charge distribution with a charging equivalent diameter, defined as the sphere with the same surface electric potential as a non-spherical particle, to calculate the particle charge fractions for fibrous aerosol particles in the continuum regime as a function of the diameter (minor axis) and major-to-minor axis ratio. Han et al. (Han et al., 1991b; Han & Gentry, 1993, 1994) produce estimates of the mean charge and free molecular flux of ions to cylindrical particles using trajectory simulations valid for instances wherein the ion mean free path is much larger than the particle length scale (i. e.) the free molecular regime of charging. Biskos et al. (Biskos et al., 2004, 2005) used Monte Carlo simulations to show that non-spherical particles acquire a higher charge than volume equivalent spheres when exposed to unipolar ions in the transition regime – instances of the ion motion being neither completely driven by diffusion nor entirely determined by ion's mass or inertia.

Gopalakrishnan, Meredith, et al. (2013) used ergodic Langevin Dynamics (LD) simulations to calculate the steady-state bipolar charge distribution on non-spherical aerosol particles in the transition regime and found that non-spherical particles acquire higher levels of elementary charge compared to spheres having the same electrical mobility and that β_i strongly depends on shape for chain-like open structures, and is weakly sensitive to shape for relatively compact or sphere-like particles. Gopalakrishnan et al. (Gopalakrishnan et al., 2011, 2013b) showed that the ratio between a length scale descriptor for the particle shape and the ion's mean persistence path is used to define the diffusive Knudsen number Kn_D of mass transfer: $Kn_D \rightarrow 0$ represents continuum ion transport regime with respect to the particle, while $Kn_D \rightarrow \infty$ implies free molecular transport. In the finite Kn_D transition regime of aerosol particle charging (Thajudeen et al., 2012), the ion's motion is significantly influenced by both diffusional motion (at large particle-ion separations) and inertial motion (in the immediate vicinity of the particle). Fig. 1 shows a schematic representation of the Kn_D -based transport regimes of particle charging and an animation of ion trajectories in the vicinity of a non-spherical particle for $Kn_D \rightarrow 0$, $Kn_D \rightarrow \infty$ and finite Kn_D is available online along with this article. For a spherical particle, the length scale used to normalize the ion mean persistence path is, naturally, the radius/diameter for the entire Kn_D regime. For non-spherical particles, continuum transport ($Kn_D \rightarrow 0$) is described using the Smoluchowski radius R_s , defined as the radius of the sphere with the same diffusion-limited transport

rate as the non-spherical particle (Kim & Torquato, 1991; Northrup et al., 1984; Potter et al., 1996; Rubinstein & Torquato, 1988; Torquato & Avellaneda, 1991; Zhou, 1995; Zhou et al., 1994) – R_s is also invoked to calculate capacitance of shapes (Chang, 1981; Chang & Laframboise, 1976; Filippov, 1994; Laframboise & Chang, 1977) in the context of momentum transfer, where it is referred to as the hydrodynamic radius. On the other hand, the free molecular transport ($Kn_D \rightarrow \infty$) of ions is described using gas kinetic theory (Vincenti & Kruger, 1975) invoking the orientation averaged projected area PA of the particle (particle-ion collision cross section). Gopalakrishnan et al. (Gopalakrishnan et al., 2011, 2013b) showed that a length scale derived as the ratio of the free molecular to the continuum length scales is suitable for describing the effect of shape on charging across the entire Kn_D regime: R_s , PA can be evaluated using efficient algorithms for any given shape (Gopalakrishnan et al., 2011; Pease et al., 2010, 2011; Shvartsburg et al., 2007; Thajudeen et al., 2012). Using LD calculations of the particle-ion collision kernel β_i and scaling analysis, Gopalakrishnan, Thajudeen, et al. (2013) produced an expression for β_i valid for particles of *arbitrary* shape and across the *entire* Kn_D regime, from continuum to free molecular, for instances of combined *repulsive Coulomb-attractive image* potential interactions encountered in unipolar diffusion charging involving collisions between neutral/like charged particles and ions. For *spherical* particles, the effect of particle-ion potential interactions – Coulomb potential (Chahl & Gopalakrishnan, 2019; Gopalakrishnan & Hogan, 2012), image potential (Ouyang et al., 2012) and combined Coulomb-image potential (Gopalakrishnan, Thajudeen, et al., 2013; Li et al., 2020) have been parameterized in prior work and produce excellent agreement with experimentally measured unipolar and bipolar charge distributions (Li et al., 2020). However, currently, there is not an analogous model to describe the combined *attractive Coulomb-image* potential interactions encountered in the bipolar diffusion charging of *non-spherical* particles involving collisions between oppositely charged particles and ions. We *hypothesize* that the β_i model described by Li et al. (2020) that parameterizes the effect of combined *attractive Coulomb-image* potential across the entire Kn_D regime for *spherical* particles may be extended for *any* shape by using the particle shape length scale descriptors R_s , PA advanced by Gopalakrishnan, Thajudeen, et al. (2013). Building on the work of Li et al. (2020), the *first* objective of this article is to extend their particle-ion collision kernel β_i model to include the effect of *particle shape* on the collision between an unlike charged particle and ion. The β_i expression described in this article, when combined with the prior β_i model that captures the combined *repulsive Coulomb-image* potential interactions for any shape (Gopalakrishnan, Thajudeen, et al., 2013), provides a complete set of particle-ion collision kernel β_i expressions for *both attractive and repulsive Coulombic* interactions and *attractive image* potential interactions for particles of *arbitrary* shape. The *second* objective of this article is to compare the charge distribution predictions of the bipolar β_i model described here and the unipolar β_i model of Gopalakrishnan, Thajudeen, et al. (2013) against published bipolar charging experimental data for spheres (Johnson et al., 2020; Wiedensohler & Fissan, 1991), cylinders (Gopalakrishnan et al., 2015), linear chains (Wen et al., 1984b) and fractal aggregates (Maricq, 2008; Xiao et al., 2012) to test the accuracy of the LD-based β_i modeling approach in predicting the diffusion charging of non-spherical aerosol particles. Along with the excellent agreement of model predictions with experimental data for *spherical* particles (Adachi et al., 1985, 1987; Gopalakrishnan et al., 2015) described by Li et al. (2020), a unified diffusion charging model for *spherical* and *non-spherical* aerosol particles alike is advanced here by validating against experimental data. The presented model is appropriate to describe the *unipolar/bipolar* diffusion charging of *arbitrary* shaped aerosol particles for a wide size range, background gas pressures and ion properties.

To test the collision kernel β_i , developed previously by Gopalakrishnan, Thajudeen, et al. (2013) and Li et al. (2020) for predicting the diffusion charging distributions of arbitrary shaped particles, we elect to re-analyze the bipolar charge distribution data reported by Wiedensohler and Fissan (1991) for spherical aerosol particles in air, nitrogen and argon. The more recent experiments by Johnson et al. (2020) that report charge fractions up to particle charge levels of ± 5 for spherical particles are also used for comparison. This comparison, along with the comparisons presented in Li et al. (2020), reinforce the LD-based β_i model's accuracy to predict the diffusion charging of spheres. The bipolar diffusion charging data for gold nanorods reported by Gopalakrishnan et al. (2015), linear chain aggregates reported by Wen et al. (1984b), fractal aggregates reported by Maricq (2008) and Xiao et al. (2012) are used to probe the model's accuracy for diverse particle shapes. The calculations of the reported measured quantities are carried out using the values of ion mass and mobility, particle size and gas temperature and pressure from the same studies, as noted in the *Methods* and

Table I-A

Summary of prior experimental studies of unipolar diffusion charging of non-spherical aerosol particles.

Reference	Short summary
Vomela and Whitby (1967)	Copper oxide and smoke aggregates ($N_p = 10 - 300$, $d_p \sim 0.043 \mu\text{m}$) acquire $\sim 70\%$ more charge than mobility equivalent spheres.
Davison et al. (1986)	Mean charge on dry actinolite fibers ($d_p = 0.3 - 0.4 \mu\text{m}$, $\frac{l_p}{d_p} \sim 7 - 10$) is $\sim 50\%$ higher than expectations for spherical particles of the same diameter.
Yu et al. (1987)	Mean charge on asbestos fibers ($d_p \sim 0.3 \mu\text{m}$, $l_p \sim 3 \mu\text{m}$) investigated in the range of $N_0 t \sim 10^{12} - 10^{13} \frac{\text{s}}{\text{m}^3}$.
Han et al. (1991a)	Charging efficiency of carbon fibers ($d_p \sim 3 \mu\text{m}$, $l_p \sim 1000 \mu\text{m}$) measured.
Oh et al. (2004)	Mean charge on TiO_2 aggregates ($D_f \sim 1.7 - 2.0$, $d_{me} \sim 50 - 200 \text{ nm}$) seen to be consistently higher than volume equivalent spheres.
Unger et al. (2004)	Mean charge on cubic NaCl particles (of side $0.42 - 1.1 \mu\text{m}$) is higher by to an order of magnitude than expectations of charging models for spherical particles in the range of $N_0 t \sim 10^{16} - 10^{19} \frac{\text{s}}{\text{m}^3}$.
Shin et al. (2010)	Mean charge on silver aggregates ($d_{me} \sim 75 - 200 \text{ nm}$) seen to be higher than spheres at $N_0 t \sim 2.5 \times 10^{13} \frac{\text{s}}{\text{m}^3}$.
Park et al. (2015)	Mean charge on silver nanorods ($d_p \sim 32, 48, 68 \text{ nm}$ and polydisperse lengths) seen to be higher than spherical PSL particles for $d_{me} \sim 200 - 400 \text{ nm}$.

Supplemental Information, SI section.

The remainder of this article is organized as follows: The *Methods* section summarizes the LD-based β_i model developed in prior work (Gopalakrishnan, Thajudeen, et al., 2013; Li et al., 2020) that is generalized here to particles of arbitrary shape for *attractive Coulomb-image* potential interactions by carrying out additional simulations. The testing of the hypothesis, introduced earlier, by comparing the predictions of β_i models of against additional LD calculations of β_i for non-spherical particles is also described. Subsequently, the calculation of expected aerosol particle bipolar charge distributions for each of the experimental datasets is described. The comparisons between experiments and predictions of LD-based β_i model is discussed in the *Results and Discussion*, followed by the *Conclusions* from this study. The *Supplemental Information* (SI) published along with this article presents tables of ion properties, details of charge distribution calculations and regression equations of the developed model to support the main text.

2. Methods

β_i model development: The Langevin Dynamics (LD) based β_i model for collisions between an unlike charged *spherical* particle and a point mass ion driven by *attractive Coulomb-image* potential interactions, described by Li et al. (2020), is extended to *non-spherical* shapes in this article by carrying out additional simulations for the same set of shapes used by Gopalakrishnan, Thajudeen, et al. (2013), listed in Table II–A and Table II–B. The number of spheres N was varied randomly in the range of 2–100 to cover diverse arbitrary shapes with no obvious symmetry and the fractal dimension D_f was varied between $\sim 1.7 - 2.5$ to model fractal particles produced in flame-based synthesis or DLCA aggregation processes (Friedlander, 2000). Our methodology here for β_i model development for *attractive Coulomb-image* potential interactions is same as that employed by Gopalakrishnan, Thajudeen, et al. (2013) for *repulsive Coulomb-image* potential interactions. Hence, we present a brief summary of the computational methods here without repeating all the details.

The non-dimensional particle-ion electrostatic potential energy $\phi(r)$ for spherical (Li et al., 2020) and non-spherical (Gopalakrishnan, Thajudeen, et al., 2013) particles depends on the particle shape and particle-ion separation, as well as Ψ_E and Ψ_I – the electrostatic potential energy to thermal energy ratios associated with Coulomb and image potential interactions, respectively, defined as:

$$\Psi_E = -\frac{z_p z_i e^2}{4\pi\epsilon_0 k_B T_s R_s} \quad (1a)$$

$$\Psi_I = \frac{\epsilon_r - 1}{\epsilon_r + 1} \frac{z_i^2 e^2}{4\pi\epsilon_0 k_B T_s R_s} \quad (1b)$$

Consistent with Gopalakrishnan, Thajudeen, et al. (2013), the Smoluchowski radius R_s is used in eq. (1) for scaling the electrostatic potential energies. $R_s = a_p$ for a spherical particle of radius a_p . $\Psi_E > 0$ for *attractive Coulomb* interactions between unlike charged particle and ion, while $\Psi_E < 0$ denotes *repulsive Coulomb* interaction between like charged particle and ion. The *attractive image* potential interaction $\Psi_I > 0$ depends on the particle dielectric constant ϵ_r (Jackson, 1975). The non-spherical test shapes considered here consist of ensembles of point contacting spheres listed in Table II–A and Table II–B. The particle charge z_p on an aggregate is modeled to be distributed among the N primary spheres such that each sphere carries a fractional charge, that adds up to z_p , and collectively

Table I–B

Summary of prior experimental studies of bipolar diffusion charging of non-spherical aerosol particles.

Reference	Short summary
Wen et al. (1984b) (used for model validation)	Mean charge of negatively charged γ -Fe ₂ O ₃ linear chain aggregates ($d_p \sim 0.041 - 0.081 \mu\text{m}$) reported.
Rogak and Flagan (1992)	Fraction of neutral particles among TiO ₂ aggregates of $d_p \sim 10 - 20 \text{ nm}$ is $\sim 5\%$ lower than spheres in the range of $d_{me} \sim 100 - 800 \text{ nm}$.
Maricq (2008) (used for model validation)	Singly, doubly and triply charged fractions of ethylene and diesel soot aggregates ($D_f \sim 1.9 - 2.0$, $d_p \sim 17 \text{ nm}$) reported.
Kulkarni et al. (2009) and Ku et al. (2011)	Neutral fraction among single walled carbon nanotubes ($d_p \sim 0.7 - 2.4 \text{ nm}$, $l_p > 5 \mu\text{m}$) is lower by up to an order of magnitude than expectations of models for spherical particles in the range of $d_{me} \sim 100 - 1000 \text{ nm}$.
Xiao et al. (2012) (used for model validation)	Neutral fraction of diesel soot particles ($D_f \sim 1.75$, $d_p \sim 24 \text{ nm}$) and silver aggregates ($D_f \sim 1.78$, $d_p \sim 14 \text{ nm}$) were reported to lower by $\sim 7\%$ than spheres. Fraction of singly and doubly charged $\sim 46\%$ higher than spheres for negative polarity and 32% less for positively charged particles.
Tanaka et al. (2014)	The neutral fraction of carbon nanofibers ($d_p \sim 10 - 25 \text{ nm}$, $d_{me} \sim 42 - 180 \text{ nm}$) is much lower than theoretical predictions for spheres. The fraction of singly and doubly charged particles are higher than spheres in the range of $d_{me} \sim 10 - 400 \text{ nm}$.
Gopalakrishnan et al. (2015) (used for model validation)	The fraction of neutrals and ratio of singly and doubly charged fractions of gold nanorods ($d_p \sim 17 - 43 \text{ nm}$, $\frac{l_p}{d_p} \sim 2 - 15$) reported to be similar to spheres in the range of $d_{me} \sim 50 - 70 \text{ nm}$.
Nie et al. (2017)	Charge fractions measured for crumpled graphene oxide particles are similar to those of spherical particles in the range of $d_{me} \sim 40 - 200 \text{ nm}$.

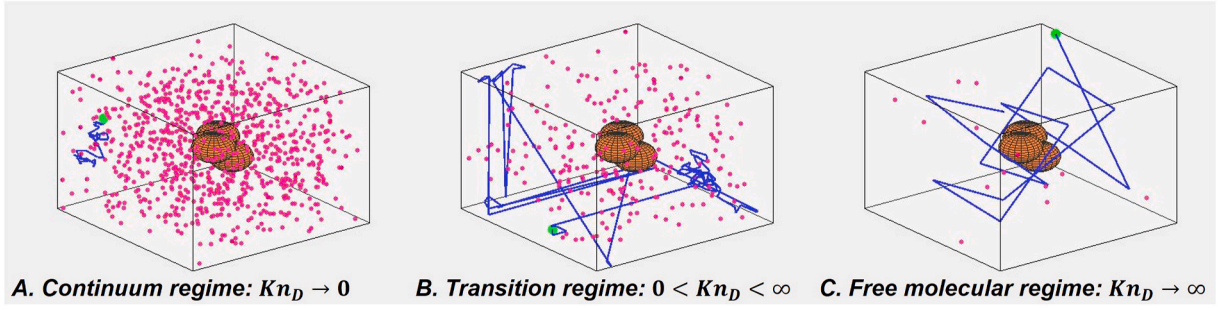


Fig. 1. Schematic illustration of the nature of ion motion (green dot) in the vicinity of a non-spherical particle (meshed particle) in the continuum, free molecular and transition regimes of diffusion charging. The smaller blue dots represent background gas molecules. Animations of the ion trajectory (shown here with blue line) is available online along with this article. (For interpretation of the references to colour in this figure legend, the reader is referred to the Web version of this article.)

minimizes the electrostatic potential energy of the particle (Brown & Hemingway, 1995), making the presented analysis applicable for *conducting* particles ($\epsilon_r \rightarrow \infty$) only; we defer the effect of particle material on the charging of non-conducting particles (finite ϵ_r) to potential future investigations. We refer the reader to Gopalakrishnan, Thajudeen, et al. (2013) for the complete form of the particle-ion potential and the calculation of the Coulombic and image forces on the ion due to a charged/neutral particle. In carrying

out simulations of ion trajectories, we neglect the effect of particle rotation by comparing the timescale of particle rotation $t_R \sim$

$2\pi \sqrt{\frac{(I_1^2 + I_2^2 + I_3^2)}{k_B T}}$ to the timescale of ion translation $t_i \sim \frac{\frac{PA}{2k_B}}{\sqrt{\frac{k_B T}{m_i}}} \frac{t_R}{t_i} \sim \sqrt{\frac{m_p}{m_i}} \gg 1$, where m_p is the particle mass and m_i is the mass of the ion. In

other words, particle rotation is much slower than the ion's translation motion and that the particle orientation with respect to the ion for determination of the image potential is likely to be minimally influenced by Brownian rotation. In this work, we specifically focus on presenting the results of LD simulations, taking into account the *attractive Coulomb-image* interactions, between non-spherical particles and singly charged ions ($z_i = \pm 1$), and investigate $\Psi_E > 0$, $\Psi_I \leq |\Psi_E|$ here.

In the continuum regime, β_i is determined by the combined electrostatic drift-diffusion of the ions to a non-spherical particle (Friedlander, 2000; Fuchs, 1963):

$$\beta_i = 4\pi \frac{k_B T_E}{f_i} R_s \eta_c(\Psi_E, \Psi_I) \quad (2)$$

f_i is the ion friction factor that can be calculated from ion self-diffusion coefficient D_i (Friedlander, 2000) and the Stokes-Einstein relation ($f_i = \frac{k_B T_E}{D_i}$) or the low-field ion mobility μ_i ($f_i = \frac{z_i e}{\mu_i}$). R_s is the Smoluchowski radius, the continuum length scale described in the *Introduction*. $\eta_c(\Psi_E, \Psi_I)$, the continuum enhancement factor, is evaluated analytically for spherical particles as (Fuchs, 1963):

$$\eta_c(\Psi_E, \Psi_I) = \begin{cases} \frac{\Psi_E}{1 - \exp(-\Psi_E)}, & \Psi_I = 0 \\ \left(\int_1^\infty \frac{1}{r^2} \exp(\phi(r)) dr \right)^{-1}, & \Psi_I \neq 0 \end{cases} \quad (3)$$


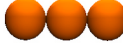
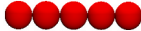





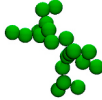
Here, $\phi(r) = -\frac{\Psi_E}{r} - \frac{\Psi_I}{2r^2(r^2-1)}$ for a spherical particle, where r is the non-dimensional separation between the particle and ion (measured in multiples of the particle radius a_p). Using trajectory simulations that neglects the ion inertia ($m_i \frac{d\vec{V}_i}{dt} = 0$) and assuming

instant thermal relaxation with the background gas ($\frac{1}{2} m_i v_i^2 = \frac{3}{2} k_B T_g$), Gopalakrishnan, Thajudeen, et al. (2013), as described in the *Supplemental Information* section of that paper, show that $\eta_c(\Psi_E, \Psi_I)$ for non-spherical particles is accurately described by eq. (3) in instances of *repulsive Coulomb-image* ($\Psi_E \leq 0$, $\Psi_I \leq |\Psi_E|$) potential interactions. Fig. 2 shows that $\eta_c(\Psi_E, \Psi_I)$, calculated using the same methodology for non-spherical particle shapes (aggregates of point contacting spheres with number of primary particles $N \leq 20$ listed in Table II–A), in instances of $0 < \Psi_E \leq 60$, $0 \leq \frac{\Psi_I}{\Psi_E} \leq 1$ is accurately described by eq. (3) accurately within $\pm 10\%$. Due to prohibitive computational expense of carrying out $[\eta_c(\Psi_E, \Psi_I)]_C$ calculations for aggregates with $N > 20$, we used an alternate approach of solving the steady state drift-diffusion equation in the absence of fluid convection to calculate the ion flux onto a non-spherical particle to calculate $\eta_c(\Psi_E, \Psi_I)$:

$$0 = -\nabla \cdot (-D_i \nabla n_i - n_i \mu_i \nabla \phi) \quad (4a)$$

Table II-A

Summary of test shapes (point contacting spheres containing N identical spheres) used along with symbols used for plotting η_c , η_f , H calculations considering both Coulomb and image potential interactions. R_s , PA for each shape are calculated using the algorithms presented in the *Supplemental Information* of Gopalakrishnan et al. (2011). Fractal pre-factor $k_f = 1.3$ for all shapes considered.






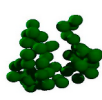
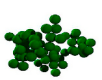

Shape	Image	$\frac{R_s}{a_p}$	$\frac{PA}{a_p^2}$	$\frac{PA}{\pi R_s^2}$	Symbol used to denote the shape in Figs. 2–6
$N = 2$ linear chain		1.39	5.80	0.96	Filled upper triangle, red
$N = 3$ linear chain		1.72	8.46	0.91	Filled lower triangle, blue
$N = 5$ linear chain		2.32	13.78	0.81	Filled square, green
$N = 5$, $D_f = 1.78$		2.19	13.28	0.88	Filled square, blue
$N = 10$ linear chain		3.59	27.07	0.67	Filled diamond, green
$N = 10$, $D_f = 1.78$		3.03	24.72	0.86	Filled diamond, blue
$N = 10$, $D_f = 2.50$		2.58	21.10	0.99	Filled diamond, red
$N = 20$ linear chain		5.79	53.66	0.51	Filled hex, dark gray
$N = 10$, $D_f = 1.78$		5.79	53.66	0.79	Filled hex, dark pink

Eq. (4a) is solved using the commercial package COMSOL® subject to the boundary conditions that $n_i(r \rightarrow \infty) = n_{i\infty}$ far away from the non-spherical particle and that the ion concentration on the surface of the particle is zero ($n_i|_p = 0$). The coordinates of the primary spheres that constitute the aggregate shapes listed in Table II-B and the charge distribution among the primary spheres, calculated using the potential energy minimization procedure described in Gopalakrishnan, Thajudeen, et al. (2013), is used to calculate the non-spherical particle-ion potential $\phi(r)$ – the image potential was not included ($\Psi_I = 0$) for simplicity. The ion concentration profile around the particle is used to evaluate the continuum enhancement factor $\eta_c(\Psi_E, \Psi_I = 0)$:

$$\eta_c(\Psi_E, \Psi_I = 0) = \frac{-D_i \nabla n_i|_p}{4\pi D_i R_s} \quad (4b)$$

Table II-B

Summary of test shapes (point contacting spheres containing N identical spheres) used along with symbols. Used for plotting η_c , η_f , H calculations considering only Coulomb potential interaction. R_s , PA for each shape are calculated using the algorithms presented in the *Supplemental Information* section of [Gopalakrishnan et al. \(2011\)](#). Fractal pre-factor $k_f = 1.3$ for all shapes considered.

Shape	Image	$\frac{R_s}{a_p}$	$\frac{PA}{a_p^2}$	$\frac{PA}{\pi R_s^2}$	Symbol used to denote the shape in Figs. 2–6
$N = 30, D_f = 1.67$		5.47	68.92	0.73	Filled circle, red
$N = 50, D_f = 2.00$		6.22	100.55	0.83	Filled circle, blue
$N = 80, D_f = 1.95$		8.13	155.91	0.75	Filled circle, green
$N = 60, D_f = 1.63$		8.35	139.29	0.64	Filled circle, yellow
$N = 45, D_f = 1.78$		6.50	98.18	0.74	Filled circle, dark pink
$N = 65, D_f = 2.32$		6.14	111.19	0.94	Filled circle, dark gray
$N = 70, D_f = 2.04$		7.18	133.74	0.83	Filled circle, dark green
$N = 100, D_f = 1.89$		9.28	199.54	0.74	Filled circle, black
$N = 100$ linear chain		19.88	260.9	0.21	Filled circle, dark blue

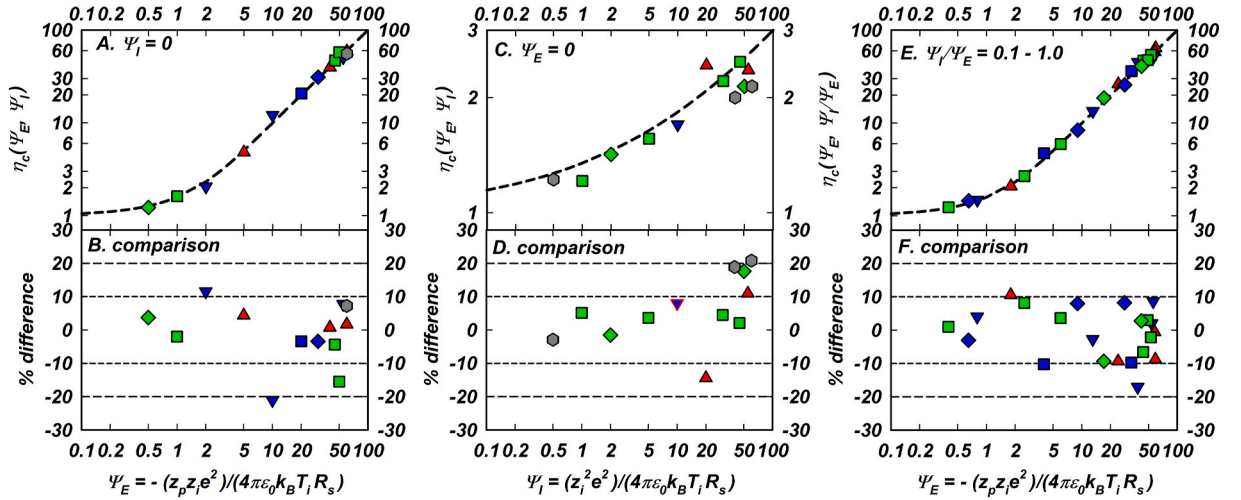


Fig. 2. Calculations of the continuum enhancement factor $\eta_c(\Psi_E, \Psi_I)$ for different test shapes listed in Table II-A for cases of A) pure Coulomb interaction between the particle and ion ($\Psi_I = 0$) plotted as a function of Ψ_E ; C) pure image interaction ($\Psi_E = 0$) plotted as a function of Ψ_I ; and E) combined Coulomb-image potential interaction ($0 < \frac{\Psi_I}{\Psi_E} \leq 1$) plotted as a function of Ψ_E . In panels A, C and E, the analytically computed η_c using eq. (3) is shown as a black dashed line. Panels B ($\Psi_I = 0$), D ($\Psi_E = 0$) and F ($0 < \frac{\Psi_I}{\Psi_E} \leq 1$), show, respectively, the % difference defined as $\left(1 - \frac{[\eta_c(\Psi_E, \Psi_I)]_C}{[\eta_c(\Psi_E, \Psi_I)]_{eq,3}}\right)\%$ between the numerically computed continuum enhancement factor $[\eta_c(\Psi_E, \Psi_I)]_C$ and the analytically computed continuum enhancement $[\eta_c(\Psi_E, \Psi_I)]_{eq,3}$. Reference lines at $\pm 10\%$, $\pm 20\%$ are included in panels B, D, F.

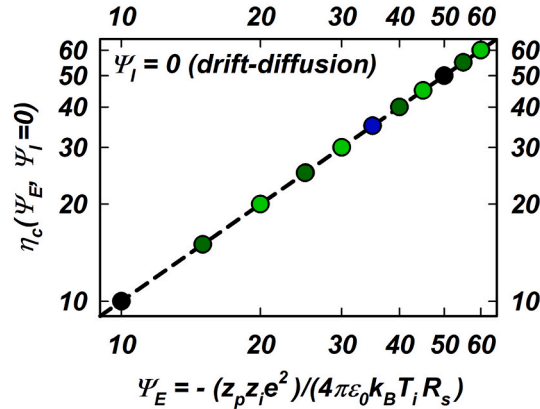


Fig. 3. Calculations of the continuum enhancement factor $\eta_c(\Psi_E, \Psi_I)$ for different test shapes listed in Table II-B for cases of pure Coulomb interaction between the particle and ion ($\Psi_I = 0$) plotted as a function of Ψ_E . The analytically computed η_c using eq. (3) is shown as a black dashed line.

n_i has a steady state solution in instances where the ion transport has spherical symmetry in the limit of $r \rightarrow \infty$. Thus, the presented analysis is applicable for isotropic diffusional charging of particles without the presence of external electric fields and/or fluid convection. Fig. 3 presents $[\eta_c(\Psi_E, \Psi_I = 0)]_{COMSOL}$ in the range of $0 < \Psi_E \leq 60$, $\Psi_I = 0$ for the point-contact aggregate shapes listed in Table II-B with $20 < N \leq 100$. $[\eta_c(\Psi_E, \Psi_I = 0)]_{eq,3}$ agrees with $[\eta_c(\Psi_E, \Psi_I = 0)]_{COMSOL}$ within round-off error $< 0.01\%$, showing the equivalence of the analytic approach (eq. (3)), the trajectory simulation approach of Gopalakrishnan, Thajudeen, et al. (2013) and the solutions to the ion drift-diffusion equation of continuum mass transport (eq. (4)).

In the free molecular regime of ion transport, characterized by the ion mean persistence path being much larger than the particle size, β_i is calculated using kinetic theory as (Allen, 1992; Mott-Smith & Langmuir, 1926; Vincenti & Kruger, 1975):

$$\beta_i = \bar{c} P A \eta_f(\Psi_E, \Psi_I) \quad (5)$$

$\bar{c} = \left(\frac{8k_B T_g}{\pi m_i} \right)^{1/2}$ is the mean thermal speed of the ions and PA is the orientation-averaged projected area of the particle. Analogous to $\eta_c(\Psi_E, \Psi_I)$, $\eta_f(\Psi_E, \Psi_I)$ is the enhancement in the particle-ion hard-sphere collision cross-section PA . For a spherical particle, $PA = \pi a_p^2$ and $\eta_f(\Psi_E, \Psi_I)$ for combined attractive or repulsive Coulomb-image potential interactions is calculated as (Allen, 1992; Mott-Smith & Langmuir, 1926; Ouyang et al., 2012):

$$\eta_f = \begin{cases} \exp(\Psi_E), \Psi_E \leq 0, \Psi_I = 0 \\ 1 + \Psi_E, \Psi_E \geq 0, \Psi_I = 0 \\ \int_{v=0}^{v=\infty} 2v^3 \exp(-v^2) [b_c(v, \Psi_E, \Psi_I)]^2 dv, \Psi_I \neq 0 \end{cases} \quad (6)$$

v is the non-dimensional speed of the ion, normalized by $\left(\frac{2k_B T_g}{m_i} \right)^{1/2}$, and b_c is the dimensionless critical radial impact parameter (normalized by particle radius a_p) defined as the minimum value of the radial impact parameter for a given set of v, Ψ_E, Ψ_I values for which particle-ion collisions occur, described in detail elsewhere (Gopalakrishnan, Thajudeen, et al., 2013; Ouyang et al., 2012). Using trajectory simulations that track ion motion in vacuum ($p_g = 0$) by neglecting the thermal diffusion and drag force on ions ($-f_i \vec{v}_i = 0$), Gopalakrishnan, Thajudeen, et al. (2013), as described in the *Supplemental Information* section of that paper, show that $\eta_f(\Psi_E, \Psi_I)$ for non-spherical particles is accurately described by eq. (6) for repulsive Coulomb ($\Psi_E < 0$) and attractive image ($\Psi_I \leq |\Psi_E|$) potential interactions. Fig. 4 shows that $\eta_f(\Psi_E, \Psi_I)$, calculated using the same methodology for non-spherical particle shapes listed in Table II-A, is described by eq. (6) accurately within 10% in instances of $0 < \Psi_E \leq 60$, $0 \leq \frac{\Psi_I}{|\Psi_E|} \leq 1$. The % difference is one-sided and was seen to $\rightarrow 0$ as the time step used for simulation is made progressively smaller; $[\eta_f(\Psi_E, \Psi_I)]_C$ follows the analytical trend of eq. (6) well and is taken to be described by the same. Due to prohibitive computational expense of carrying out $[\eta_f(\Psi_E, \Psi_I)]_C$, calculations for aggregates with $N > 20$, we did not carry out simulations with the more complex aggregates listed in Table II-B.

Eq. (2) and eq. (5) represent the continuum and free molecular limits of β_i with R_s and PA , respectively, as the corresponding length scale descriptors of particle shape. As mentioned in the *Introduction*, R_s, PA can be evaluated using efficient algorithms (Gopalakrishnan et al., 2011; Pease et al., 2010, 2011; Shvartsburg et al., 2007; Thajudeen et al., 2012) for any given shape or from prior regressions for aggregates (Thajudeen et al., 2012) and cylinders (Hansen, 2004). The enhancement factors $\eta_c(\Psi_E, \Psi_I)$ and $\eta_f(\Psi_E, \Psi_I)$ for any particle shape is described by the analytic expressions for spherical shape, eq. (3) and eq. (6) respectively, with Ψ_E, Ψ_I defined by eq. (1). Regressions for the calculation of η_c, η_f in the range of $-60 \leq \Psi_E \leq 60$, $0 \leq \frac{\Psi_I}{|\Psi_E|} \leq 1$ are given in Sec. S1, SI.

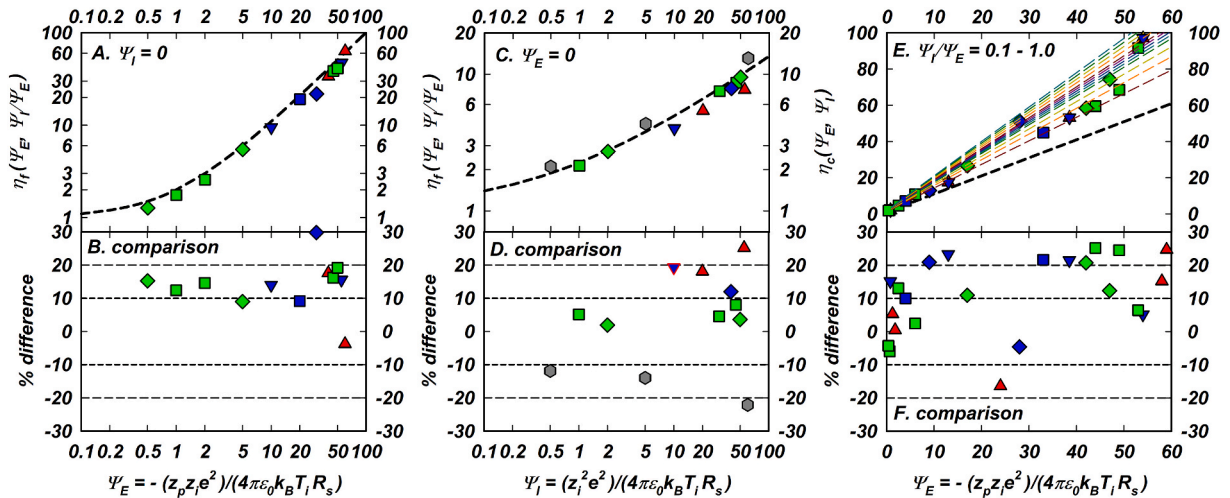


Fig. 4. Calculations of the free molecular enhancement factor $\eta_f(\Psi_E, \Psi_I)$ for different test shapes listed in Table II-A for cases of A) pure Coulomb interaction between the particle and ion ($\Psi_I = 0$) plotted as a function of Ψ_E ; C) pure image interaction ($\Psi_E = 0$) plotted as a function of Ψ_I ; and E) combined Coulomb-image potential interaction ($0 < \frac{\Psi_I}{|\Psi_E|} \leq 1$) plotted as a function of Ψ_E . In panels A, C and E, the analytically computed η_f using eq. (6) is shown as a black dashed line. Panel E also displays the analytically computed η_f curves (increasing as the lines move vertically upward) using eq. (6) for $0 < \frac{\Psi_I}{|\Psi_E|} \leq 1$ without individual labels. Panels B ($\Psi_I = 0$), D ($\Psi_E = 0$) and F ($0 < \frac{\Psi_I}{|\Psi_E|} \leq 1$), show, respectively, the % difference defined as $\left(1 - \frac{[\eta_f(\Psi_E, \Psi_I)]_C}{[\eta_f(\Psi_E, \Psi_I)]_{eq.6}} \right) \%$ between the numerically computed continuum enhancement factor $[\eta_f(\Psi_E, \Psi_I)]_C$ and the analytically computed continuum enhancement $[\eta_f(\Psi_E, \Psi_I)]_{eq.6}$. Reference lines at $\pm 10\%, \pm 20\%$ are included in panels B, D, F.

Following Gopalakrishnan, Thajudeen, et al. (2013), scaling the collision kernel β_i using the length scale $L_H = \left(\left(\frac{PA\eta_f}{\pi} \right)^2 \frac{1}{R_s\eta_c} \right)^{\frac{1}{3}}$ and the ion relaxation time $\frac{m_i}{f_i}$ as a reference timescale, yields a non-dimensional collision kernel H :

$$H = \frac{\beta_i m_i}{f_i L_H^3} \quad (7a)$$

Likewise, $L_{Kn} = \frac{PA\eta_f}{R_s\eta_c}$, derived as the ratio of the effective free molecular particle-ion collision cross section $PA\eta_f$ and continuum diffusion radius $R_s\eta_c$, is used to non-dimensionalize the ion thermal energy $k_B T_g$ to derive the diffusive Knudsen number Kn_D as:

$$Kn_D = \frac{\sqrt{m_i k_B T_g}}{f_i L_{Kn}} \quad (7b)$$

$\frac{\sqrt{m_i k_B T_g}}{f_i}$ is the ion mean persistence path describing ion transport length scale and is compared to the particle length scale L_{Kn} to establish the diffusional transport regime of ions from free molecular to continuum transport. Eq. (2) and eq. (5) are scaled using the definitions of eq. (7) to yield the continuum ($Kn_D \rightarrow 0$) and free molecular ($Kn_D \rightarrow \infty$) limits, respectively:

$$Kn_D \rightarrow 0 : H = 4\pi Kn_D^2 \quad (8a)$$

$$Kn_D \rightarrow \infty : H = \sqrt{8\pi} Kn_D \quad (8b)$$

A model for H or non-dimensional β_i valid for particles of arbitrary shape, as a function of Kn_D, Ψ_E, Ψ_I for the entire $0 < Kn_D < \infty$ regime was derived by Gopalakrishnan, Thajudeen, et al. (2013) for repulsive Coulomb-image interactions ($-\infty < \Psi_E \leq 0, \Psi_I \leq |\Psi_E|$):

$$H(Kn_D, \Psi_E, \Psi_I) = \frac{4\pi Kn_D^2 + 25.836 Kn_D^3 + \sqrt{8\pi} Kn_D (11.211 Kn_D^3)}{1 + 3.502 Kn_D + 7.211 Kn_D^2 + 11.211 Kn_D^3} \quad (9)$$

Eq. (9) converges to the limits defined by eq. (8a) and (8b), respectively, as $Kn_D \rightarrow 0$ and $Kn_D \rightarrow \infty$. In prior work, eq. (9) has been shown to be valid to describe the hard sphere ($\Psi_E = \Psi_I = 0$) collisions between a spherical (Gopalakrishnan & Hogan, 2011) or arbitrary shaped (Gopalakrishnan et al., 2011) particle and a point mass as well as between two arbitrary shaped particles (Thajudeen et al., 2012), the repulsive Coulomb potential ($-\infty < \Psi_E \leq 0, \Psi_I = 0$) mediated collisions between a like charged particle-ion or

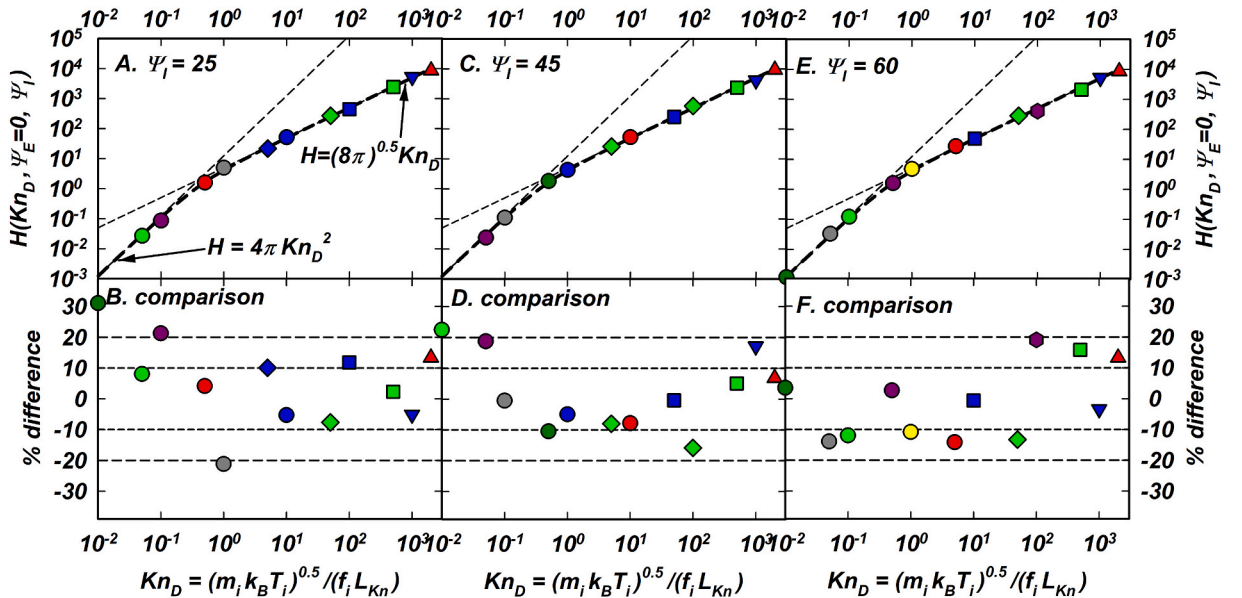


Fig. 5. Calculations of the non-dimensional collision kernel $H(Kn_D, \Psi_E, \Psi_I)$ for different test shapes listed in Table II–A and B for cases of pure image interaction ($\Psi_E = 0$) plotted as a function of the diffusive Knudsen number Kn_D for A) $\Psi_I = 25$; C) $\Psi_I = 45$; and E) $\Psi_I = 60$. In panels A, C and E, the continuum limit (eq. (8a)) and free molecular limit (eq. (8b)) of H is shown using light black dashed lines with labels. Also shown using dark black dashed line is eq. (9), a model for $H(Kn_D, \Psi_E, \Psi_I)$ that is valid for hard sphere and short-range potential (such as image) interactions. Panels B ($\Psi_I = 25$), D ($\Psi_I = 45$) and F ($\Psi_I = 60$), show, respectively, the % difference defined as $\left(1 - \frac{[H(Kn_D, \Psi_E, \Psi_I)]_{LD}}{[H(Kn_D, \Psi_E, \Psi_I)]_{eq.9}} \right) \%$ between the numerically computed continuum enhancement factor $[H(Kn_D, \Psi_E, \Psi_I)]_{LD}$ and the analytically computed continuum enhancement $[H(Kn_D, \Psi_E, \Psi_I)]_{eq.9}$. Reference lines at $\pm 10\%, \pm 20\%$ are included in panels B, D, F.

particle-particle (Gopalakrishnan & Hogan, 2012), and also describes the *image* potential interaction between a neutral particle and an ion ($\Psi_E = 0, \Psi_I$) when the enhancement factors $\eta_c(\Psi_E = 0, \Psi_I)$, $\eta_f(\Psi_E = 0, \Psi_I)$ are calculated appropriately (Ouyang et al., 2012). Thus, for describing the unipolar (like charged particle and ion collision of either polarity) and neutral particle-ion interactions for any particle shape, eq. (8) may be used to calculate H or β_i as a function of Kn_D, Ψ_E, Ψ_I using particle and ion properties along with gas pressure and temperature in eq. (1) and eq. (7).

Li et al. (2020) analyzed *attractive Coulomb-image* potential influenced collisions between *spherical* particles and ions for $0 < \Psi_E \leq 60, 0 \leq \frac{\Psi_I}{\Psi_E} \leq 1, 0 < Kn_D \leq 2000$. By parameterizing the particle-ion collision time distributions calculated using LD, they derived $H(Kn_D, \Psi_E, \Psi_I)$ as:

$$H(Kn_D, \Psi_E, \Psi_I) = e^h H_{HS}(Kn_D) \quad (10a)$$

$$\mu(Kn_D, \Psi_E, \Psi_I) = \frac{C}{A} \left(1 + k \frac{\ln Kn_D - B}{A} \right)^{-\frac{1}{k-1}} \exp \left(- \left(1 + k \frac{\ln Kn_D - B}{A} \right)^{-\frac{1}{k-1}} \right), \quad k \neq 0 \quad (10b)$$

Regression fits to calculate A, B, C, k as a function of Ψ_E, Ψ_I developed by Li et al. (2020) are repeated with permission in Sec. S2, SI. It was shown that the LD-based model (eq. (10a) and eq. (10b), collectively referred to as eq. (10) hereon) describes H to within nominally $\pm 10\%$ for instances of *spherical* particle-ion collisions where both Coulombic and image forces are significant. In total, eq. (9) and eq. (10) may be used to calculate β_i 's required to calculate the complete *bipolar* charge distributions (with like charged and unlike charged particle-ion collisions) or *unipolar* charge distributions (with only like charged particle-ion collisions) for *spherical* and *non-spherical* particles, pending verification of the applicability of eq. (10) for *attractive Coulomb-image* collisions between non-spherical particles and ions.

Using the LD simulation methodology to calculate $H(Kn_D, \Psi_E, \Psi_I)$ described in the *Supplemental Information* of Gopalakrishnan, Thajudeen, et al. (2013), we carried out simulations for the particle shapes listed in both Table II–A and B. Firstly, for the case of an uncharged particle and ion ($\Psi_E = 0$), Fig. 5 displays $H(Kn_D, \Psi_E = 0, \Psi_I)$ for $0.01 \leq Kn_D \leq 2000$. The % difference between the predictions of eq. (9) and the LD-computed H is no more than $\pm 20\%$ for all the shapes considered, with the symmetric scatter about 0 attributed to statistical variation associated with LD methodology (Gopalakrishnan & Hogan, 2011). The good agreement suggests that eq. (9) may be used to calculate β_i for uncharged non-spherical particle-ion collisions, across the entire Kn_D regime. Fig. 6 displays

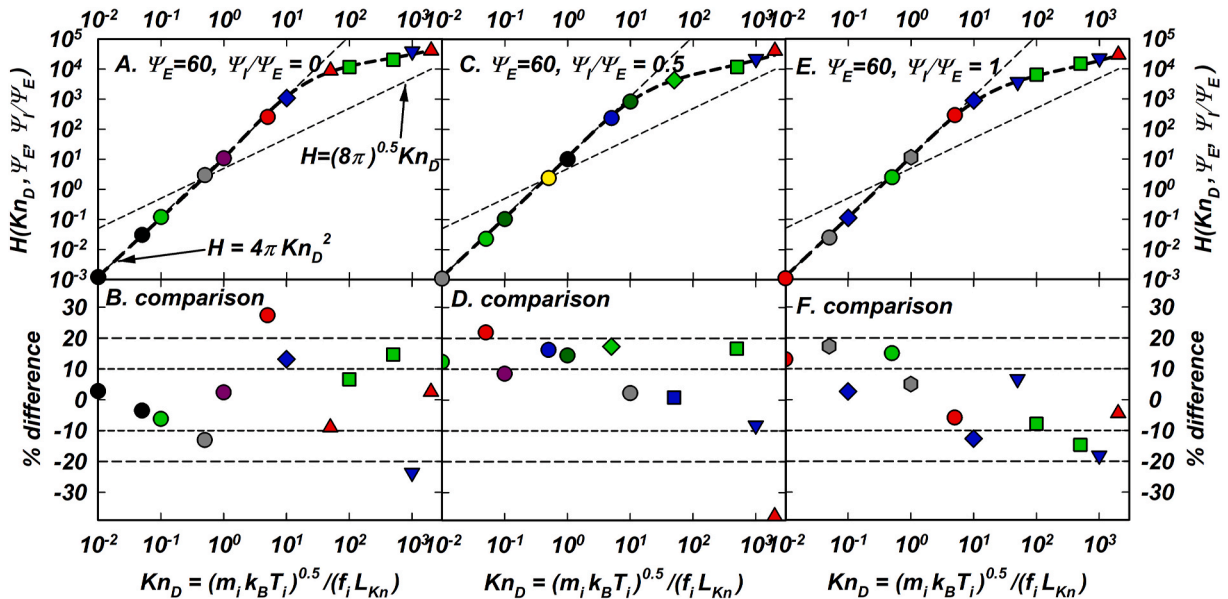


Fig. 6. Calculations of the non-dimensional collision kernel $H(Kn_D, \Psi_E, \Psi_I)$ for different test shapes listed in Table II–A and B for cases of combined Coulomb and image interaction ($0 < \Psi_E \leq 1$) plotted as a function of the diffusive Knudsen number Kn_D for $\Psi_E = 60$ and A) $\frac{\Psi_I}{\Psi_E} = 0$; C) $\frac{\Psi_I}{\Psi_E} = 0.5$; and E) $\frac{\Psi_I}{\Psi_E} = 1$. In panels A, C and E, the continuum limit (eq. (8a)) and free molecular limit (eq. (8b)) of H is shown using light black dashed lines with labels. Also shown using dark black dashed line is eq. (10), a model for $H(Kn_D, \Psi_E, \Psi_I)$ valid for combined attractive Coulomb-image potential interactions. Panels B ($\frac{\Psi_I}{\Psi_E} = 0$), D ($\frac{\Psi_I}{\Psi_E} = 0.5$) and F ($\frac{\Psi_I}{\Psi_E} = 1$), show, respectively, the % difference defined as $\left(1 - \frac{[H(Kn_D, \Psi_E, \Psi_I)]_{LD}}{[H(Kn_D, \Psi_E, \Psi_I)]_{eq.10}} \right) \%$ between the numerically computed continuum enhancement factor $[H(Kn_D, \Psi_E, \Psi_I)]_{LD}$ and the analytically computed continuum enhancement $[H(Kn_D, \Psi_E, \Psi_I)]_{eq.10}$. Reference lines at $\pm 10\%, \pm 20\%$ are included in panels B, D, F.

$H(Kn_D, \Psi_E, \Psi_I)$ for $\Psi_E = 60$ for the shapes listed in Table II–A and B. At low and high Kn_D , $[H(Kn_D, \Psi_E, \Psi_I)]_{LD}$ approaches the continuum (eq. (8a)) and free molecular (eq. (8b)) limits, respectively. At the edge of the fitting intervals, $\Psi_E \sim 60$ and $Kn_D \sim 2000$, errors accrued in curve fitting lead to one sided difference that may be important for collision kernel calculation in instances of highly charged particles colliding with oppositely charged ions at very low pressure. Such instances, relevant for charging in low pressure conditions will require future efforts to expand the range of Ψ_E and Kn_D to mitigate the error due to regression. Similarly, Fig. S1, SI and Fig. S2, SI show $H(Kn_D, \Psi_E, \Psi_I)$ for $\Psi_E = 30$ and $\Psi_E = 7$, respectively. It is seen that eq. (10) is a satisfactory model of β_i to describe *attractive Coulomb-image* interactions between non-spherical particles and point mass ions in the $0 < Kn_D \leq 2000$ regime for potential energy ratios $0 < \Psi_E \leq 60$, $0 \leq \frac{\Psi_I}{\Psi_E} \leq 1$. Figures 4, 5, S1, SI and S2, SI, together show that R_s, PA describe non-spherical particle shape and allow the expression of the collision kernel β_i in a non-dimensional, shape invariant form $H(Kn_D, \Psi_E, \Psi_I)$. As a combination, eq. (9) and eq. (10), are valid for any shape of particle, and for both *attractive* and *repulsive Coulombic* interactions while also taking into account the *image* potential. It is now desirable to test the predictions of the same against experimental data of diffusion charging of non-spherical particles. Bipolar diffusion charging involves the calculation of collision kernels for both like charged and unlike charged particle-ion collisions and serves as a test for both eq. (9) (unipolar kernel) and eq. (10) (bipolar kernel).

Calculation of bipolar charge distributions for comparison: The steady state fraction f_p of particles, of known shape and dimensions, carrying p charges exposed to a population of singly charged positive and negative ions is calculated as:

$$f_p = \begin{cases} \frac{\prod_{j=p}^{j=-1} \left(\frac{\sum_{k=1}^{NEG} \beta_{j+1,k-} \theta_{k-}}{\sum_{i=1}^{POS} \beta_{j,i+} \theta_{i+}} \right)}{\Sigma}, & p \leq -1 \\ \frac{1}{\Sigma}, & p = 0 \\ \frac{\prod_{j=1}^{j=p} \left(\frac{\sum_{i=1}^{POS} \beta_{j-1,i+} \theta_{i+}}{\sum_{k=1}^{NEG} \beta_{j,k-} \theta_{k-}} \right)}{\Sigma}, & p \geq 1 \end{cases} \quad (11a)$$

$$\Sigma = \sum_{p=-\infty}^{p=-1} \left\{ \prod_{j=p}^{j=-1} \left(\frac{\sum_{k=1}^{NEG} \beta_{j+1,k-} \theta_{k-}}{\sum_{i=1}^{POS} \beta_{j,i+} \theta_{i+}} \right) \right\} + 1 + \sum_{p=1}^{p=\infty} \left\{ \prod_{j=1}^{j=p} \left(\frac{\sum_{i=1}^{POS} \beta_{j-1,i+} \theta_{i+}}{\sum_{k=1}^{NEG} \beta_{j,k-} \theta_{k-}} \right) \right\} \quad (11b)$$

Here, $\beta_{p,i\pm}$ is the collision kernel between a particle carrying p charges and the i^{th} type of \pm ion out of POS and NEG number of distinct types. In prior work (Boisdrón & Brock, 1970; Adachi et al., 1985), eq. (11) was derived for diffusion charging of particles by a single type of positive ion and a singly type of negative ion. We have generalized the steady charge balance on a population of mono-sized particles to interact with multiple types of positive and negative ions via eq. (11). It has been common to assume a single kind of positive and negative ion each of average mass and mobility derived empirical correlations (Vohra et al., 1969; Mohnen, 1974) to interpret measured charge fractions in prior experimental work on spherical (Adachi et al., 1985, 1987) and non-spherical (Wen et al., 1984b; Maricq, 2008; Xiao et al., 2012) particles: $POS = NEG = 1$ and $\theta_+ = \theta_- = 0.5$ for comparing with measurements of f_p . Using tandem ion mobility spectrometry-mass spectrometry, recent reports (Gopalakrishnan et al., 2013a, 2015; Maißer et al., 2015; Liu et al., 2020) of the mass and mobility distribution and chemical composition of positive and negative ions involved in the diffusion charging of aerosol particles can be easily incorporated into eq. (11), wherever such data is available. $\sum_{i=1}^{POS} \beta_{j,i+} \theta_{i+}$ represents the concentration-weighted contribution of each type of positive ion to the total charging rate: $R_{p \rightarrow p+1} = n_p n_{T+} \sum_{i=1}^{POS} \beta_{j,i+} \theta_{i+}$. Likewise, $R_{p \rightarrow p-1} = n_p n_{T-} \sum_{k=1}^{NEG} \beta_{j,k-} \theta_{k-}$ capturing the decrease in particle charge due to collisions between particles and all of the NEG types of negative ions. Recent work by Carsí and Alonso (2020) examines the influence of a population of heterogenous ions, including the distributions in their mass, electrical mobility and loss rate due to recombination and diffusion to walls, on particle charging. The bipolar charge fractions f_p obtained via eq. (11) self-consistently accounts for the increase/decrease of particle charge by collision with heterogenous negative/positive ions and are used for evaluating the β_i models of eq. (9) and eq. (10). Li et al. (2020) compared the charge distributions calculated using eq. (9) and eq. (10) in eq. (11) for *spherical* particles and found excellent agreement (within $\pm 20\%$) with experimental data for both unipolar (Adachi et al., 1985, 1987) and bipolar (Adachi et al., 1985; Gopalakrishnan et al., 2015) diffusion charging. As indicated in Table I–B and in the Introduction, we elect to compare bipolar charge distribution predictions (using eq. (11) with eqs. (9) and (10)) against experiments for diverse particle shapes and background gases. The charge fraction f_p reported by these experimental studies, with the exception of Wen et al. (1984b), are compared directly with model predictions obtained via eq. (11) with eq. (9) and eq. (10) for β_i . Sec. S3, SI summarizes the ion properties used for calculating theoretical expectations of bipolar charge fractions – these inputs are either the same values used by the original authors to analyze their experimental data or (in the case of Johnson et al. (2020)) those that match the experimental conditions closely and may be considered to be reasonable estimates of the ion properties. In all of our comparisons except for the dataset of Johnson et al. (2020), the total concentration of positive and negative charge carriers is assumed to be equal: $n_{T+} = n_{T-}$. For Johnson et al. (2020), $\frac{n_{T+}}{n_{T-}} \cong 1.2$ as shown in Table S3–B, SI. The details of particle length scales R_s and PA calculations for the aggregate charging data of Maricq (2008) and Xiao et al. (2012) are presented in Sec. S4, SI and for the cylinders charging data of Gopalakrishnan et al. (2015) are presented in Sec. S5, SI. Wen et al. (1984b) report their measured bipolar charge distributions as mean particle charge p as a function of the electrical

mobility classification voltage (1–10 kV) applied in the experimental runs. Sec. S6, SI describes the steps to calculate p by considering the convolution of the aerosol particle charge distribution f_p (eq. (11)) with β_i given by eq. (9) and eq. (10)) and the DMA transfer function (Knutson & Whitby, 1975; Stolzenburg & McMurry, 2008). In the next section, we discuss the comparisons with experiment and assess the accuracy of the LD-based β_i model of eq. (9) and eq. (10).

3. Results and discussion

3.1. Comparison with bipolar charging data for spherical particles

In addition to the comparisons done by Li et al. (2020), we present comparisons that further establish the validity of the LD-based β_i model (eq. (9) and eq. (10)) for spherical particles. Fig. 7 presents experimental data and theoretical predictions, for the dataset reported by Wiedensohler and Fissan (1991) for spherical 5–100 nm silver and NaCl particles in air. The theoretical predictions are calculated using two sets of ion properties extracted from the original work (Wiedensohler & Fissan, 1991) – set 1 and set 2, listed in

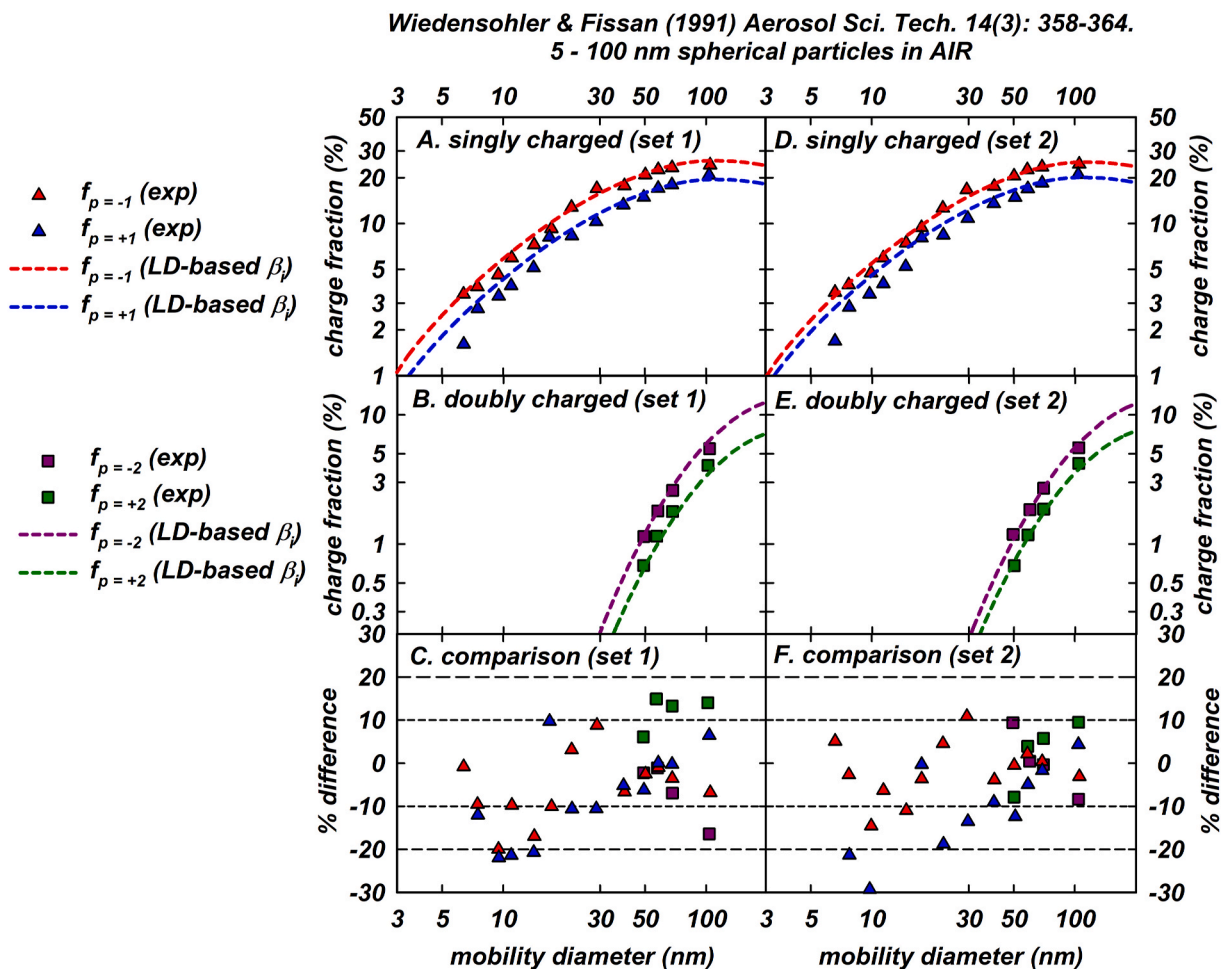


Fig. 7. Calculations of the bipolar charge distribution for experimental data reported by Wiedensohler and Fissan (1991) Aerosol Sci. Tech. 14 (3): 358–364 for 5–100 nm spherical silver and NaCl particles in air. The ion properties used for model calculations using eq. (11) with the LD-based β_i (eq. (9) and eq. (10)) for set 1 and set 2 are tabulated in Tables S3–A, SI. Panel A (“set 1”) and panel D (“set 2”) show singly charged fraction of positive polarity (red filled triangles for experimental data and red dashed lines for model predictions) and negative polarity (blue filled triangles for experimental data and blue dashed lines for model predictions). Similarly, panel B (“set 1”) and panel E (“set 2”) show doubly charged fraction of positive polarity (dark pink squares for experimental data and dark pink dashed lines for model predictions) and negative polarity (dark green squares for experimental data and dark green dashed lines for model predictions). Panel C (“set 1”) and panel F (“set 2”) show the % difference, defined as $\left(1 - \frac{f_p^{\text{eq 11}}}{f_p^{\text{exp}}}\right) \%$, between experimental data and model predictions for both singly and doubly charged fraction of particles. Reference lines at $\pm 10\%$, $\pm 20\%$ are shown in panels C and F. In all model calculations, the particles are assumed to be conducting ($\epsilon_r \rightarrow \infty$). (For interpretation of the references to colour in this figure legend, the reader is referred to the Web version of this article.)

Tables S3–A, SI. The calculated singly charged fractions of both positive polarity and negative polarity and the corresponding doubly charged fractions follow the experimental data closely. The % difference between most of the predictions and the experimental data for $p = \pm 1, \pm 2$ fall within $\pm 10\%$, indicating excellent agreement of predictions with experiments. Apart from the statistical uncertainty associated with the LD simulation methodology (Gopalakrishnan & Hogan, 2011), an under-prediction of smaller size (higher electrical mobility) particles is seen in the comparison. Sub-10 nm particles have comparable mobility to the charging ions in ambient charging conditions and the calculation of particle-ion collision kernel in such instances require the modeling of both particle and ion diffusional motion. The LD simulations carried out to develop eq. (9) and eq. (10) assumed the particle motion to be negligible compared to ion motion and may introduce a difference that scales inversely with particle size. However, in the other datasets considered in this article as well as the prior comparisons discussed by Li et al. (2020), such under-prediction was absent and unbiased, symmetric spread about 0 is seen. Fig. S3, SI shows a similar comparison for charging data in nitrogen (using two sets of ion properties: set 1 and set 2, also listed in Table S3-B, SI) with the % difference in this case being higher than in the case of charging in air. The predictions qualitatively capture the experimental trend satisfactorily, with % differences evenly spread about 0 and up to $\sim \pm 35\%$ with the experimental data, again pointing to unbiased predictions by the LD-based β_i model. Lastly, Fig. S4, SI plots predictions and experimental data for charging in argon (ion properties tabulated in Table S3-C, SI) and shows excellent agreement, nominally within $\pm 10\%$. Fig. 8 presents a comparison of the measured neutral fraction and predictions (two sets of ion properties were used for model calculations as noted in Sec. S3-D, SI) for 50–200 nm spherical silver particles, reported by Xiao et al. (2012). For this dataset, the predictions of the LD-based β_i model are within $\sim \pm 5\%$, showing excellent agreement and accuracy of the model. In bipolar charging experiments, the neutral fraction is measured with a lower level of uncertainty relative to the measurement of higher charge fractions – this is due to the fact that for sub-200 nm particles, the fraction of charged particles is low to begin with and acquiring sufficient particle counts of higher charge states is often limited by the concentration output of the nanoparticle generation technique used. This leads to a corresponding higher uncertainty on the measured fractions of higher charged states. Considering this practical difficulty, we note that for neutral fraction (with low uncertainty), our predictions nearly exactly match the data. For higher order charge fractions, the agreement is satisfactory and without any bias.

Recently, Johnson et al. (2020) developed a tandem technique that uses an aerodynamic aerosol classifier (AAC) coupled to a differential mobility analyzer (DMA) to measure the fraction of charge states up to ± 6 for aerosol nanoparticles. Fig. 9 presents the fraction of charge particles f_p for $p = -5$ to $p = 5$ for 46–598 nm spherical DOS particles (except for 598 nm particles for whom $p = \pm 6$ is also plotted). The ion properties used for model calculations, calculated using the ion mobility measurements reported by Leppä et al. (2017), are described and tabulated in Sec. S3-B, SI. The lower charge states ($p = -2, -1, 0, +1, +2$) and charge states up to $p = \pm 5$ in most cases are well described by the LD-based β_i model to within $\pm 10\%$. For 358 and 598 nm particles show deviations beyond 20% for $p = 4, 5, 6$ but show excellent agreement for $p = -6, -5, -4$. This one-sided deviation may be due to the high uncertainty or low number concentration of these charge states during the experiments and warrant further examination in future work. The collisions between particles with $p = 4 - 6$ and negative ions lead to $0.05 < Kn_D < 0.12$, $0.93 < \Psi_E < 2.44$, and between positive ions lead to $0.10 < Kn_D < 0.35$, $-2.44 < \Psi_E < -0.93$, that are well within the range of the validity of eq. (10) ($0 < Kn_D \leq 2000$, $0 \leq \Psi_E \leq 60$). Further, we assume that DOS particles are perfectly conducting in our analysis and find excellent agreement for the

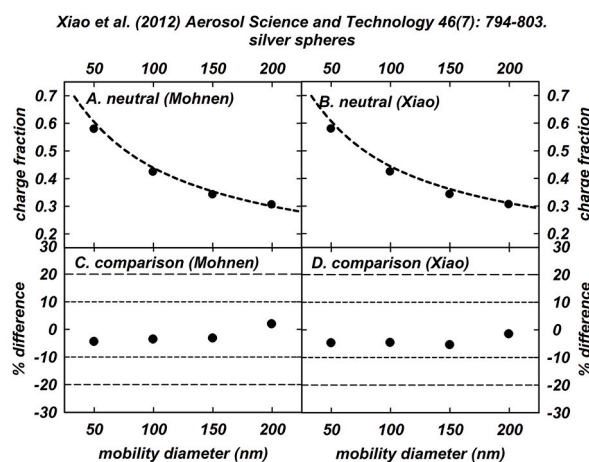


Fig. 8. Calculations of the bipolar charge distribution for experimental data reported by Xiao et al. (2012) Aerosol Sci. Tech. 46 (7): 764–803 for 50–200 nm spherical silver particles in air. The ion properties used for model calculations using eq. (11) with the LD-based β_i (eq. (9) and eq. (10)) for “Mohnen” and “Xiao” are tabulated in Sec. S3-D, SI. Panel A (“Mohnen”) and panel B (“Xiao”) show neutral fraction (black filled circles for experimental data and black dashed line for model predictions). Panel C (“Mohnen”) and panel D (“Xiao”) show the % difference, defined as $\left(1 - \frac{f_p^{\text{eq.11}}}{f_p^{\text{exp}}}\right) \%$, between experimental data and model predictions. Reference lines at $\pm 10\%$, $\pm 20\%$ are shown in panels C and D. In all model calculations, the particles are assumed be conducting ($\epsilon_f \rightarrow \infty$).

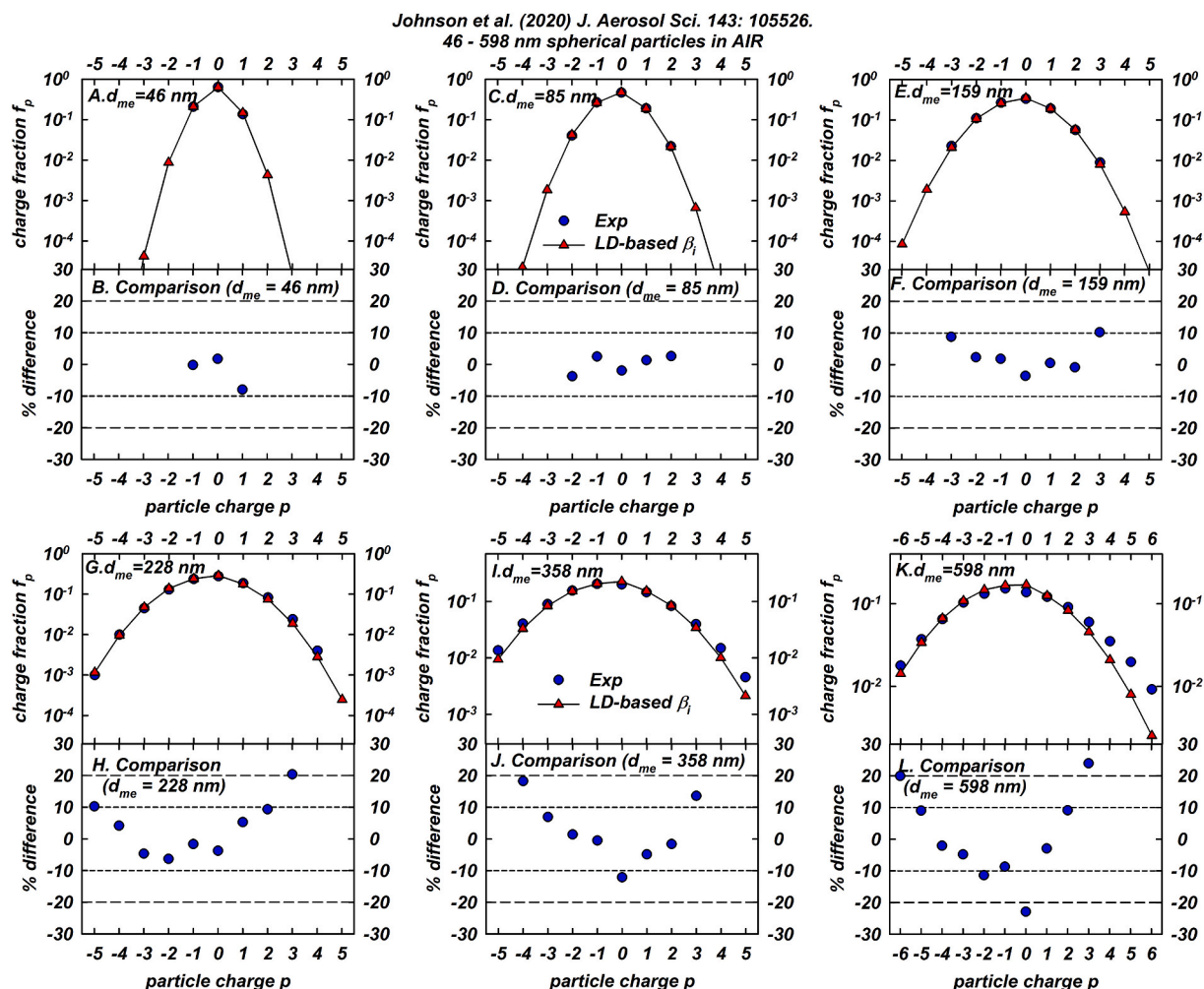


Fig. 9. Calculations of the bipolar charge distribution for experimental data reported by Johnson et al. (2020) J. Aerosol Sci. 143: 105526 for 46 – 598 nm spherical DOS particles in air. The ion properties used for model calculations using eq. (11) with the LD-based β_i (eq. (9) and eq. (10)) are tabulated in Sec. S3-B, SI. The fraction of particles carrying p charges is plotted as a function of p for A) $d_p = 46$ nm, C) $d_p = 85$ nm, E) $d_p = 159$ nm, G) $d_p = 228$ nm, I) $d_p = 358$ nm, K) $d_p = 598$ nm. The experimental data is shown using blue filled circles and the model predictions are shown using red filled triangles connected by straight lines in black. Panel B (" $d_p = 46$ nm"), panel D (" $d_p = 85$ nm"), panel F (" $d_p = 159$ nm"), panel H (" $d_p = 228$ nm"), panel J (" $d_p = 358$ nm"), panel L (" $d_p = 598$ nm") show the % difference, defined as $\left(1 - \frac{f_p^{eq,11}}{f_p^{exp}}\right)\%$, between experimental

data and model predictions. Reference lines at $\pm 10\%$, $\pm 20\%$ are shown in panels B, D, F, H, J and L. In all model calculations, the particles are assumed to be conducting ($\epsilon_r \rightarrow \infty$). (For interpretation of the references to colour in this figure legend, the reader is referred to the Web version of this article.)

lower charge states ($-1 \leq p \leq 1$) for which the effect of material is expected to be most important (collision between a neutral particle and ion). Hence, it is reasonable to attribute the differences seen for the higher order positive charge fractions ($4 \leq p \leq 6$) for 358 and 458 nm data sets to possible experimental issues and construe the excellent agreement for $-6 \leq p \leq -4$ as evidence for robust behavior of the LD-based β_i model. Lastly, Fig. 10 (panels I–L) present charge fractions for 10–400 nm poly (α -olefin) oligomer (PAO) oil droplets in air. Panel L plots the % difference between the predictions (made using ion properties listed in Sec. S3-E, SI). It is seen that most of the data points are within $\pm 10\%$ and the remaining are nominally within $\pm 20\%$, further vindicating the ability of the LD-based β_i model in predicting the charging of spheres. Taken together, Figs. 7–9, S3, S4 and the prior work of Li et al. (2020) show that the LD-based β_i model is accurate for the bipolar diffusion charging of 5–1000 nm spherical, conducting aerosol particles, and the comparisons with experiments provide validation in the range of $-46.4 < \Psi_E < 46.4$ and $0.09 < Kn_D < 58.4$ (see Table III-A). Their extension to non-conducting (finite ϵ_r) particles is a potential future investigation that will allow the examination of the effect of particle material on diffusion charging. Their applicability for non-spherical, conducting particles is next.

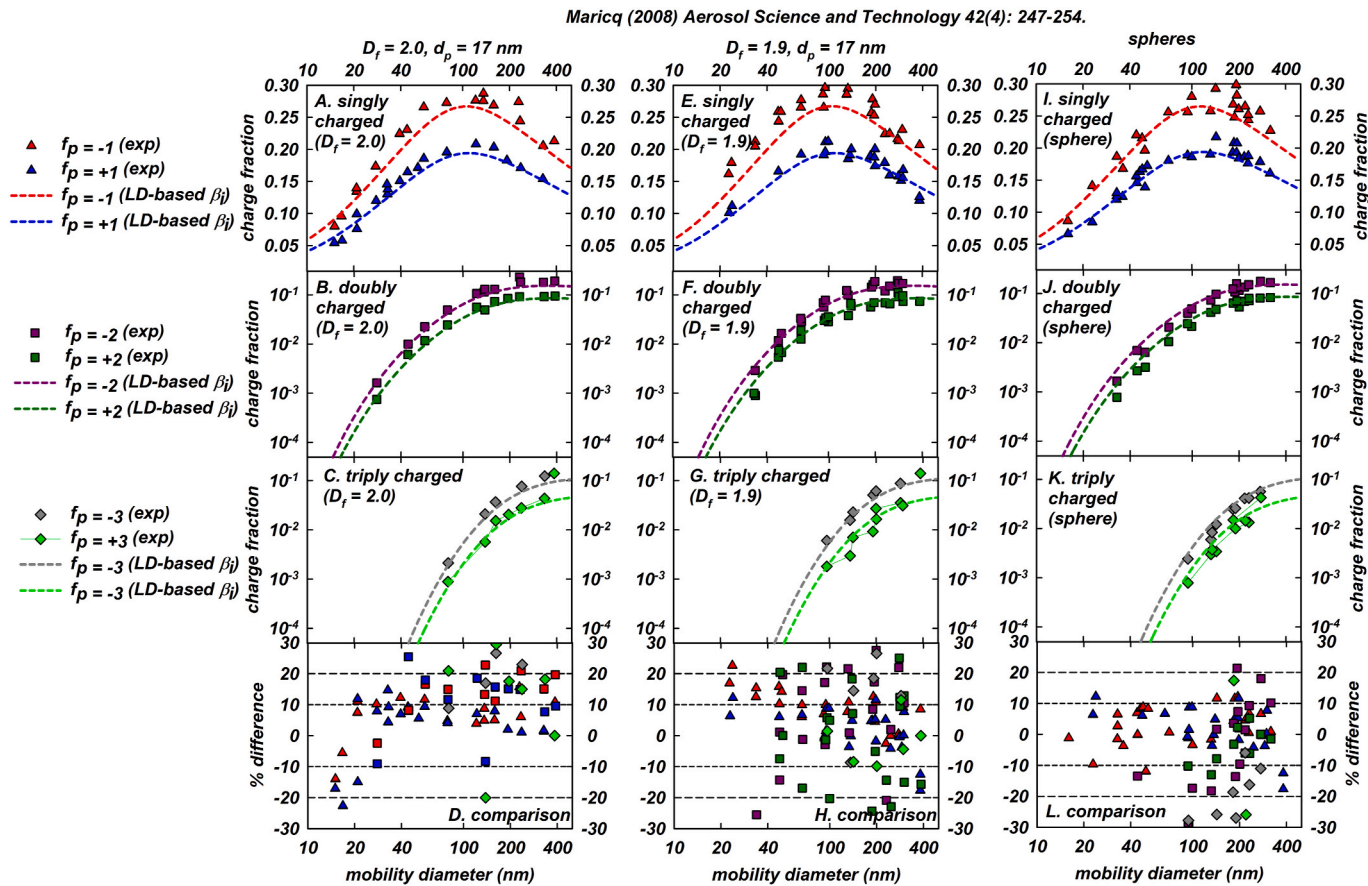


Fig. 10. Calculations of the bipolar charge distribution for experimental data reported by Maricq (2008) Aerosol Sci. Tech. 42 (4): 247–254 for flame generated fractal aggregates (of fractal dimension $D_f \sim 2.0, 1.9$ and primary particle diameter $d_p \sim 17$ nm) and PAO spherical particles in air. The ion properties used for model calculations using eq. (11) with the LD-based β_i (eq. (9) and eq. (10)) are tabulated in Sec. S3-E, SI. Steps for calculation of length scales R_s and PA from measured quantities for the aggregate charging data is described in Sec. S4, SI. Panel A ($D_f = 2.0$, $d_p = 17$ nm), panel E ($D_f = 1.9$, $d_p = 17$ nm), and panel I (PAO spherical particles) show singly charged fraction of positive polarity (red filled triangles for experimental data and red dashed lines for model predictions) and negative polarity (blue filled triangles for experimental data and blue dashed lines for model predictions). Similarly, panel B ($D_f = 2.0$, $d_p = 17$ nm), panel F ($D_f = 1.9$, $d_p = 17$ nm), and panel J (PAO spherical particles) show doubly charged fraction of positive polarity (dark pink filled squares for experimental data and dark pink dashed lines for model predictions) and negative polarity (dark green filled squares for experimental data and dark green dashed lines for model predictions). Lastly, panel D ($D_f = 2.0$, $d_p = 17$ nm), panel H ($D_f = 1.9$, $d_p = 17$ nm), and panel I (PAO spherical particles) the

% difference, defined as $\left(1 - \frac{f_p^{eq,11}}{f_p^{exp}}\right)\%$, between experimental data and model predictions for both singly, doubly and triply charged fraction of particles. Reference lines at $\pm 10\%$, $\pm 20\%$ are shown in panels D, H and L. In all model calculations, the particles are assumed be conducting ($\epsilon_r \rightarrow \infty$). (For interpretation of the references to colour in this figure legend, the reader is referred to the Web version of this article.)

Table III-A

Estimates of nominal Ψ_E (eq. (1a)) and Kn_D (eq. (7b)) ranges for the experimental data of the bipolar charging of spherical particles using average ion properties listed in Sec. S3-F, SI.

Reference	Figure #	Ψ_E		Kn_D	
		Min	Max	Min	Max
Wiedensohler and Fissan (1991) (NaCl and silver spheres)	7, S3, S4	− 46.4	46.4	0.22	58.4
Xiao et al. (2012) (silver spheres)	8	− 4.52	4.52	0.09	1.62
Maricq (2008) (PAO droplets)	11 (panels I–L)	− 6.97	6.97	0.09	4.76
Johnson et al. (2020) (DOS droplets $d_p = 46$ nm)	9 (panels A, B)	− 12.1	12.1	0.39	3.92
Johnson et al. (2020) (DOS droplets $d_p = 85$ nm)	9 (panels C, D)	− 6.55	6.55	0.25	1.51
Johnson et al. (2020) (DOS droplets $d_p = 159$ nm)	9 (panels E, F)	− 3.50	3.50	0.16	0.59
Johnson et al. (2020) (DOS droplets $d_p = 228$ nm)	9 (panels G, H)	− 2.44	2.44	0.12	0.35
Johnson et al. (2020) (DOS droplets $d_p = 385$ nm)	9 (panels I, J)	− 1.56	1.56	0.09	0.19
Johnson et al. (2020) (DOS droplets $d_p = 598$ nm)	9 (panels K, L)	− 0.93	0.93	0.05	0.10
Gopalakrishnan et al. (2015) (gold spheres $d_p = 73$ nm)	Table IV	− 4.25	4.25	0.28	1.49

3.2. Comparison with bipolar charging data of quasi-fractal aggregates

Maricq (2008) reports singly, doubly and triply charged fractions of flame generated aggregates, plotted in Fig. 10, panels A–D for fractal dimension $D_f = 2.0$ and panels E–H for $D_f = 1.9$. The predictions of charge fractions follow the experimental trend closely and differ by $\sim \pm 10\%$ as can be seen from panel D and panel H for $D_f = 2.0$ and $D_f = 1.9$, respectively. Along with ion properties listed in

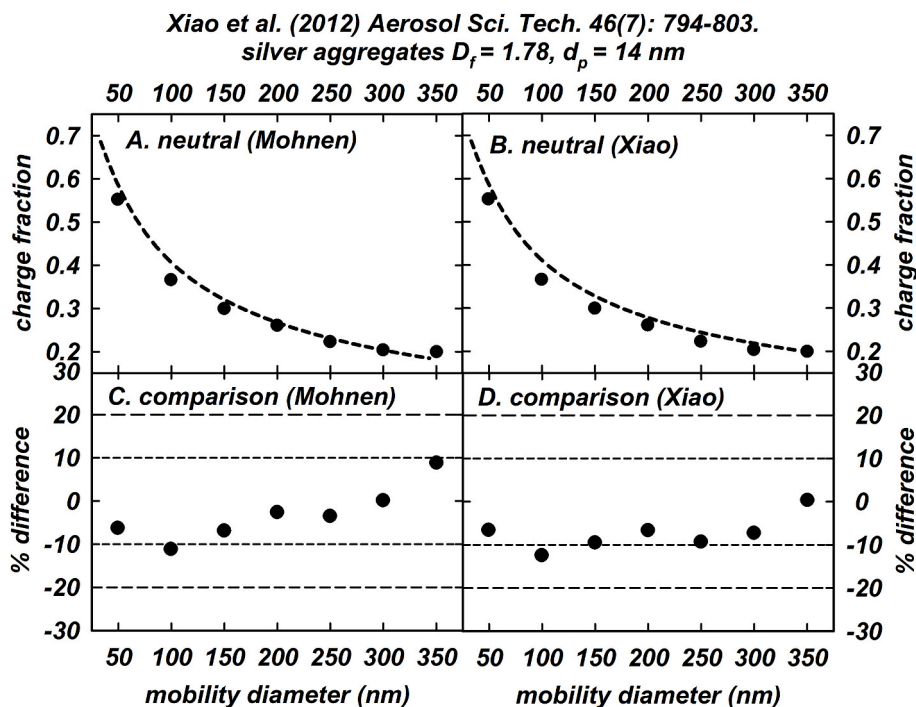


Fig. 11. Calculations of the bipolar charge distribution for experimental data reported by Xiao et al. (2012) Aerosol Sci. Tech. 46 (7): 764–803 for 50–200 nm mobility diameter silver fractal aggregate particles in air. The ion properties used for model calculations using eq. (11) with the LD-based β_i (eq. (9) and eq. (10)) for “Mohnen” and “Xiao” are tabulated in Sec. S3-D, SI. Steps for calculation of length scales R_p and PA from measured quantities for the aggregate charging data is described in Sec. S4, SI. Panel A (“Mohnen”) and panel B (“Xiao”) show neutral fraction (black filled circles for experimental data and black dashed line for model predictions). Panel C (“Mohnen”) and panel D (“Xiao”) show the % difference, defined as $\left(1 - \frac{f_p^{eq,11}}{f_p^{exp}}\right)\%$, between experimental data and model predictions. Reference lines at $\pm 10\%$, $\pm 20\%$ are shown in panels C and D. In all model calculations, the particles are assumed be conducting ($\epsilon_r \rightarrow \infty$).

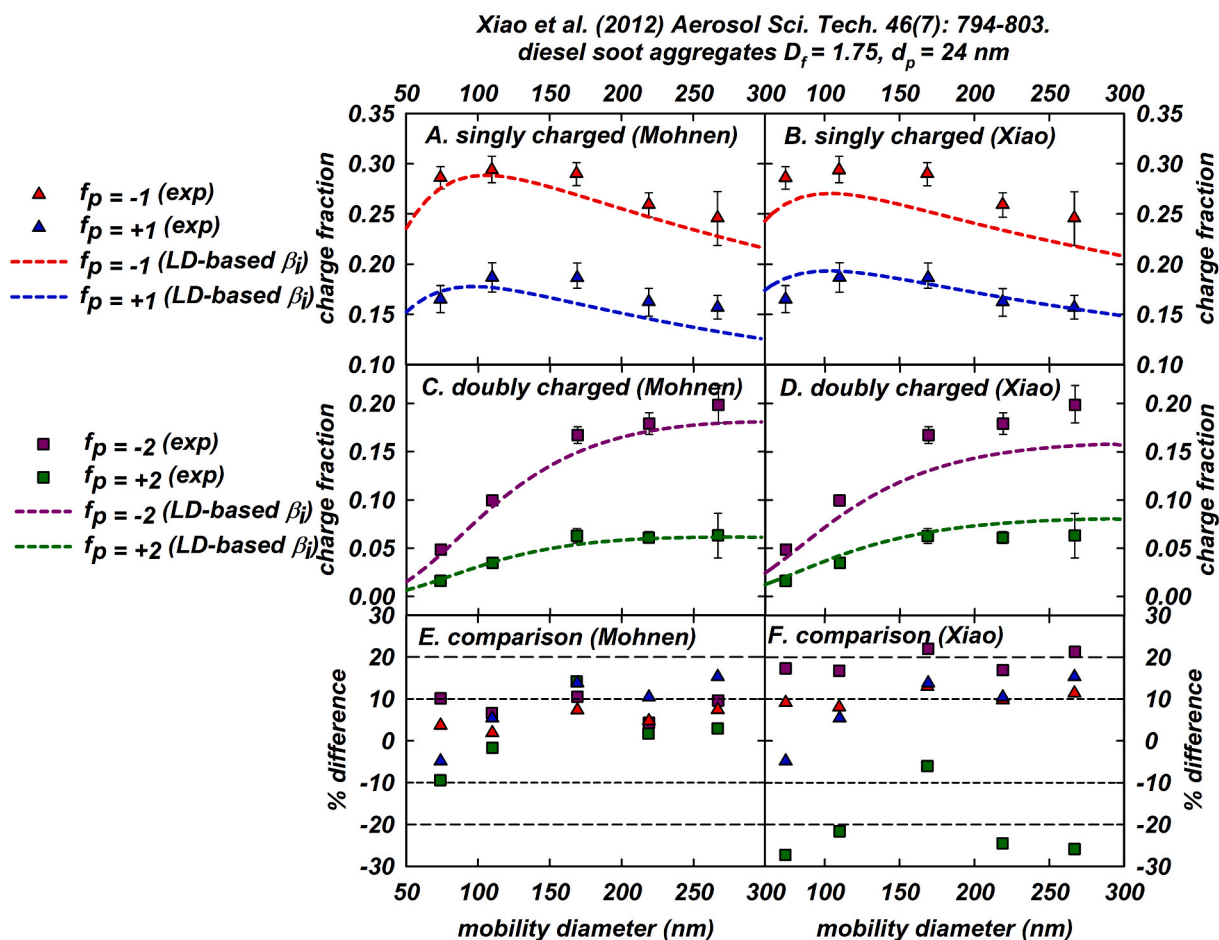


Fig. 12. Calculations of the bipolar charge distribution for experimental data reported by Xiao et al. (2012) Aerosol Sci. Tech. 46 (7): 764–803 for 50–200 nm diesel soot fractal aggregate particles in air. The ion properties used for model calculations using eq. (11) with the LD-based β_i (eq. (9) and eq. (10)) for “Mohnen” and “Xiao” are tabulated in Sec. S3-D, SI. Steps for calculation of length scales R_s and PA from measured quantities for the aggregate charging data is described in Sec. S4, SI. Panel A (“Mohnen”) and panel B (“Xiao”) show singly charged fraction of positive polarity (red filled triangles for experimental data and red dashed lines for model predictions) and negative polarity (blue filled triangles for experimental data and blue dashed lines for model predictions). Similarly, panel C (“Mohnen”) and panel D (“Xiao”) show doubly charged fraction of positive polarity (dark pink filled squares for experimental data and dark pink dashed lines for model predictions) and negative polarity (dark green filled squares for experimental data and dark green dashed lines for model predictions). Panel E (“Mohnen”) and panel F (“Xiao”) show the % difference,

defined as $\left(1 - \frac{f_p^{eq,11}}{f_p^{exp}}\right)\%$, between experimental data and model predictions for both singly and doubly charged fraction of particles. Reference lines

at $\pm 10\%$, $\pm 20\%$ are shown in panels E and F. In all model calculations, the particles are assumed be conducting ($\epsilon_r \rightarrow \infty$). (For interpretation of the references to colour in this figure legend, the reader is referred to the Web version of this article.)

Sec. S3-E, SI, Sec. S4, SI describes the calculations of R_s , PA for aggregates from experimentally reported parameters: the electrical mobility diameter D_{me} , mean primary particle diameter d_p and fractal dimension D_f inferred from TEM measurements. Consistent with Gopalakrishnan, Meredith, et al. (2013), the bipolar charging characteristics of aggregates with $D_f \sim 1.9$, 2.0 resembles that of mobility equivalent spheres. In other words, shapes that are low to moderately non-spherical do not differ significantly from mobility equivalent spheres according to model predictions and this is confirmed by similar fractions reported by Maricq’s experimental data plotted in panels A–C ($D_f = 2.0$), panels E–G ($D_f = 1.9$), and panels I–K (spheres). Xiao et al. (2012) report neutral fractions for silver aggregates ($D_f = 1.78$) that is compared against model predictions using two sets of ion properties listed in Sec. S3-D, SI and using R_s , PA calculated as described in Sec. S4, SI. Similar to the data set of silver spheres in Figs. 8 and 11 also shows excellent agreement between the predicted and measured neutral fractions. Fig. 12 presents experimental data and predictions for singly and doubly charged fractions for diesel soot aggregates ($D_f = 1.75$). It is seen that some predictions are nominally less than the measured values by $\sim 15 - 20\%$, unlike the other comparisons presented so far. In most cases, a deviation less than 10%, however an unbiased spread about 0 is lacking in these datasets. Overall, the model produces reasonable qualitative agreement for the datasets considered here

across the range of $D_f \sim 1.75 - 2.0$ and $D_{me} \sim 10 - 400$ nm. The aggregates considered here have a $\frac{PA}{\pi R_s^2}$, a measure of the degree of non-sphericity of a shape, in the range of 0.74 – 0.86: while $\frac{PA}{\pi R_s^2} = 1$ represents a perfect sphere, $\frac{PA}{\pi R_s^2} \rightarrow 0$ represents an infinite cylinder that is highly non-spherical. The comparisons described here highlight the need to acquire further experimental data for charging of low fractal dimension aggregates, preferably $D_f < 1.6$ that would lead to highly non-spherical open structures $\frac{PA}{\pi R_s^2} \ll 1$. Such shapes are expected to charge significantly differently compared to mobility equivalent spheres (Gopalakrishnan, Meredith, et al., 2013) and would provide further probing of the LD-based β_i model at low $\frac{PA}{\pi R_s^2}$ for aggregates.

3.3. Comparison with bipolar charging data of chain-like and cylindrical particles

The bipolar charge distribution of straight chain iron oxide particles composed of spherical primary particles, measured by Wen et al. (1984b), is presented as particle mean charge as a function of the DMA classification voltage in Fig. 13. The predictions are made taking into account the convolution between the charge distribution and the DMA transfer function for the experimental conditions reported as described in Sec. S6, SI. It is seen that for instances in which the DMA classification voltage > 2 kV, the % difference is between $\pm 20\%$ for most instances indicating excellent agreement for lower charge states – the low mobility particles that exit the DMA at higher voltages are well described by the model. Since particle electrical mobility $Z_p = \frac{ze}{\zeta_p}$, for particles with nominally the same

friction factor ζ_p higher charge states lead to higher electrical mobility and exit the DMA at lower voltages: $Z_{DMA} = \frac{Q_{DMA} \ln\left(\frac{r_o}{r_i}\right)}{2\pi L V_{DMA}}$. Here, Z_{DMA} is the electrical mobility of particles exiting the DMA classifier at a sheath flow of Q_{DMA} and a classification voltage of V_{DMA} , and r_o, r_i, L are the dimensions of the DMA described in detail elsewhere (Knutson & Whitby, 1975). For $V_{DMA} < 3$ kV nominally, the particles exiting the DMA are dominated by highly mobile species or highly charged particles. In these instances, the % difference is $\sim 30 - 40\%$ but no higher overall. This suggests reasonable agreement when considering the lower concentration of highly charged particles relative to particles of lower charge state. The datasets presented in Fig. 13 vindicate the ability of the LD-based model β_i model to predict the charge distribution of nearly straight chain particles.

Lastly, the bipolar charge distribution data for gold cylindrical particles reported by Gopalakrishnan et al. (2015) is compared against model predictions (using ion properties listed in Sec. S3-C, SI and R_s, PA calculated as described in Sec. S5, SI) in Table IV for $\frac{PA}{\pi R_s^2}$ in the range of 0.84 – 1.00. The overall excellent agreement (with only a few data points with % difference $> 30\%$) further verifies

Table III-B

Estimates of nominal Ψ_E (eq. (1a)) and Kn_D (eq. (7b)) ranges for the experimental data of the bipolar charging of non-spherical particles (aggregates, linear chains and cylinders) using average ion properties listed in Sec. S3-F, SI.

Reference	Figure #	$\frac{PA}{\pi R_s^2}$	Ψ_E		Kn_D	
			Min	Max	Min	Max
Maricq (2008) (diesel soot aggregates $D_f = 2.0$)	10(panels A–D)	0.86	– 7.75	7.75	0.09	5.25
Maricq (2008) (diesel soot aggregates $D_f = 1.9$)	10 (panels E–G)	0.84	– 6.32	6.32	0.10	2.94
Xiao et al. (2012) (silver aggregates $D_f = 1.78$)	11	0.74	– 4.14	4.14	0.12	1.70
Xiao et al. (2012) (flame generated aggregates $D_f = 1.75$)	12	0.78	– 2.78	2.78	0.13	0.97
Wen et al. (1984b) (iron oxide linear chains $d_p = 41$ nm)	13 (panels A, B)	0.45	–0.32	0.32	0.11	0.16
Wen et al. (1984b) (iron oxide linear chains $d_p = 51$ nm)	13 (panels C, D)	0.54	–0.47	0.47	0.13	0.20
Wen et al. (1984b) (iron oxide linear chains $d_p = 59$ nm)	13 (panels E, F)	0.50	–0.46	0.46	0.14	0.21
Wen et al. (1984b) (iron oxide linear chains $d_p = 66$ nm)	13 (panels G, H)	0.56	–0.63	0.63	0.15	0.26
Wen et al. (1984b) (iron oxide linear chains $d_p = 75$ nm)	13 (panels I, J)	0.55	–0.70	0.70	0.17	0.30
Wen et al. (1984b) (iron oxide linear chains $d_p = 81$ nm)	13 (panels K, L)	0.41	–0.56	0.56	0.19	0.31
Gopalakrishnan et al. (2015) (gold cylinders $\frac{l_p}{d_p} \sim 2.2$)	Table IV	0.84	–3.18	3.18	0.35	1.18
Gopalakrishnan et al. (2015) (gold cylinders $\frac{l_p}{d_p} \sim 4.3$)	Table IV	0.85	–6.79	6.79	0.56	3.45
Gopalakrishnan et al. (2015) (gold cylinders $\frac{l_p}{d_p} \sim 11.3$)	Table IV	0.70	–2.67	2.67	0.37	1.12
Gopalakrishnan et al. (2015) (gold cylinders $\frac{l_p}{d_p} \sim 14.9$)	Table IV	0.63	–2.66	2.66	0.40	1.23

Table IV

Calculations of the bipolar charge distribution for experimental data reported by Gopalakrishnan et al. (2015) Aerosol Sci. Tech. 49 (12): 1181–1194 for cylindrical gold particles in air. The ion properties used for model calculations using eq. (11) with β_i given by eq. (9) and eq. (10) are tabulated in Sec. S3-C, SI. The steps for calculation of length scales R_s and PA from measured quantities for the cylinder charging data is described in Sec. S5, SI. The cylinder diameter d_p (nm), length-to-diameter ratio $\frac{l_p}{d_p}$ and $\frac{PA}{\pi R_s^2}$ ratio are listed along with the mobility equivalent diameter D_{me} (nm). The neutral fraction $f_{p=0}$, the ratio of singly to doubly charged particles of both polarities $\frac{f_{p=\pm 1}}{f_{p=\pm 2}}$, the ratio of negative to positive charged particles of singly and doubly charged states $\frac{f_{p=-1}}{f_{p=+1}}, \frac{f_{p=-2}}{f_{p=+2}}$ are listed here with the superscript $(\cdot)^{exp}$ denoting experimental data and $(\cdot)^{eq.11}$ denoting model predictions. The % difference between model and experiment is quantified as $\left(1 - \frac{(\cdot)^{eq.11}}{(\cdot)^{exp}}\right)\%$. In all model calculations, particles are assumed be conducting ($\epsilon_r \rightarrow \infty$).

d_p (nm)	$\frac{l_p}{d_p}$	$\frac{PA}{\pi R_s^2}$	D_{me} (nm)	$f_{p=0}^{exp}$	$f_{p=0}^{eq.11}$	$\left(1 - \frac{(\cdot)^{eq.11}}{(\cdot)^{exp}}\right)\%$
11.2	4.3	0.84	30.9	0.80836	0.75954	6.04%
43.3	2.2	0.84	64.6	0.47912	0.46336	3.29%
17.3	14.9	0.63	68.1	0.4592	0.49851	-16.65%
20.9	11.3	0.70	70.9	0.44972	0.49834	-10.81%
73.2	1.0	1.00	73.2	0.48	0.52	-9.03%
d_p (nm)	$\frac{l_p}{d_p}$	$\frac{PA}{\pi R_s^2}$	D_{me} (nm)	$\left(\frac{f_{p=-1}}{f_{p=-2}}\right)^{exp}$	$\left(\frac{f_{p=-1}}{f_{p=-2}}\right)^{eq.11}$	$\left(1 - \frac{(\cdot)^{eq.11}}{(\cdot)^{exp}}\right)\%$
11.2	4.3	0.84	30.9	72.0274	67.64879	6.08%
43.3	2.2	0.84	64.6	11.147	7.5336	32.42%
17.3	14.9	0.63	68.1	5.5228	7.4466	-34.83%
20.9	11.3	0.7	70.9	6.7724	7.3456	-8.46%
73.2	1.0	1	73.2	7.51	8.56	-13.97%
d_p (nm)	$\frac{l_p}{d_p}$	$\frac{PA}{\pi R_s^2}$	D_{me} (nm)	$\left(\frac{f_{p=+1}}{f_{p=+2}}\right)^{exp}$	$\left(\frac{f_{p=+1}}{f_{p=+2}}\right)^{eq.11}$	$\left(1 - \frac{(\cdot)^{eq.11}}{(\cdot)^{exp}}\right)\%$
11.2	4.3	0.84	30.9	72.0274	67.64879	6.08%
43.3	2.2	0.84	64.6	11.147	7.5336	32.42%
17.3	14.9	0.63	68.1	5.5228	7.4466	-34.83%
20.9	11.3	0.7	70.9	6.7724	7.3456	-8.46%
73.2	1.0	1	73.2	7.51	8.56	-13.97%
d_p (nm)	$\frac{l_p}{d_p}$	$\frac{PA}{\pi R_s^2}$	D_{me} (nm)	$\left(\frac{f_{p=-1}}{f_{p=+1}}\right)^{exp}$	$\left(\frac{f_{p=-1}}{f_{p=+1}}\right)^{eq.11}$	$\left(1 - \frac{(\cdot)^{eq.11}}{(\cdot)^{exp}}\right)\%$
11.2	4.3	0.84	30.9	1.395	1.264222	9.37%
43.3	2.2	0.84	64.6	1.313	1.264	3.73%
17.3	14.9	0.63	68.1	0.864	1.241	-43.65%
20.9	11.3	0.7	70.9	0.95	1.232	-29.69%
73.2	1.0	1	73.2	1.24	1.2	2.96%
d_p (nm)	$\frac{l_p}{d_p}$	$\frac{PA}{\pi R_s^2}$	D_{me} (nm)	$\left(\frac{f_{p=-2}}{f_{p=+2}}\right)^{exp}$	$\left(\frac{f_{p=-2}}{f_{p=+2}}\right)^{eq.11}$	$\left(1 - \frac{(\cdot)^{eq.11}}{(\cdot)^{exp}}\right)\%$
11.2	4.3	0.84	30.9	1.433	1.617331	-12.86%
43.3	2.2	0.84	64.6	1.617	1.593	1.48%
17.3	14.9	0.63	68.1	1.237	1.556	-25.78%
20.9	11.3	0.7	70.9	1.104	1.536	-39.06%
73.2	1.0	1	73.2	1.608	1.474	8.34%

the utility of the LD-based approach to describe ion transport on to non-spherical particles facilitated by thermal energy and electrostatic interactions. For the $\frac{PA}{\pi R_s^2}$ probed in the compared experiments (Gopalakrishnan et al., 2015; Wen et al., 1984b) (0.41 – 0.84), the diffusion charging of cylinders/linear chains are well described by the LD-based β_i model (eq. (9) and eq. (10)) in the range of $-7.75 < \Psi_E < 7.75$ and $0.09 < Kn_D < 5.25$, as shown in Table III-B. As mentioned before, along with low fractal dimension aggregates, future experiments using very high length-to-diameter ratio (> 100) cylinders would be highly instructive for model evaluation at lower values of $\frac{PA}{\pi R_s^2}$. Lastly, the presented data test the model at transition regime diffusive Knudsen number range $0.1 < Kn_D < 10$, nominally. Charge fractions measured at $10^2 - 10^5$ Pa gas pressures that lead to higher $Kn_D \sim 100 - 1000$ would also provide validation in the near free molecular regime of charging.

3.4. Effect of particle shape on diffusion charging of conducting aerosol particles

The LD-based β_i model (eq. (9) and eq. (10)), shown to describe the charging of spherical and non-spherical particles (Figs. 2–6) has been tested using experimental data from the literature in Figs. 7–13. The LD-based β_i model is used here to probe the effect of particle

Wen et al. (1984) J. Aerosol Sci. 15(2): 103-122.
straight chain agglomerates

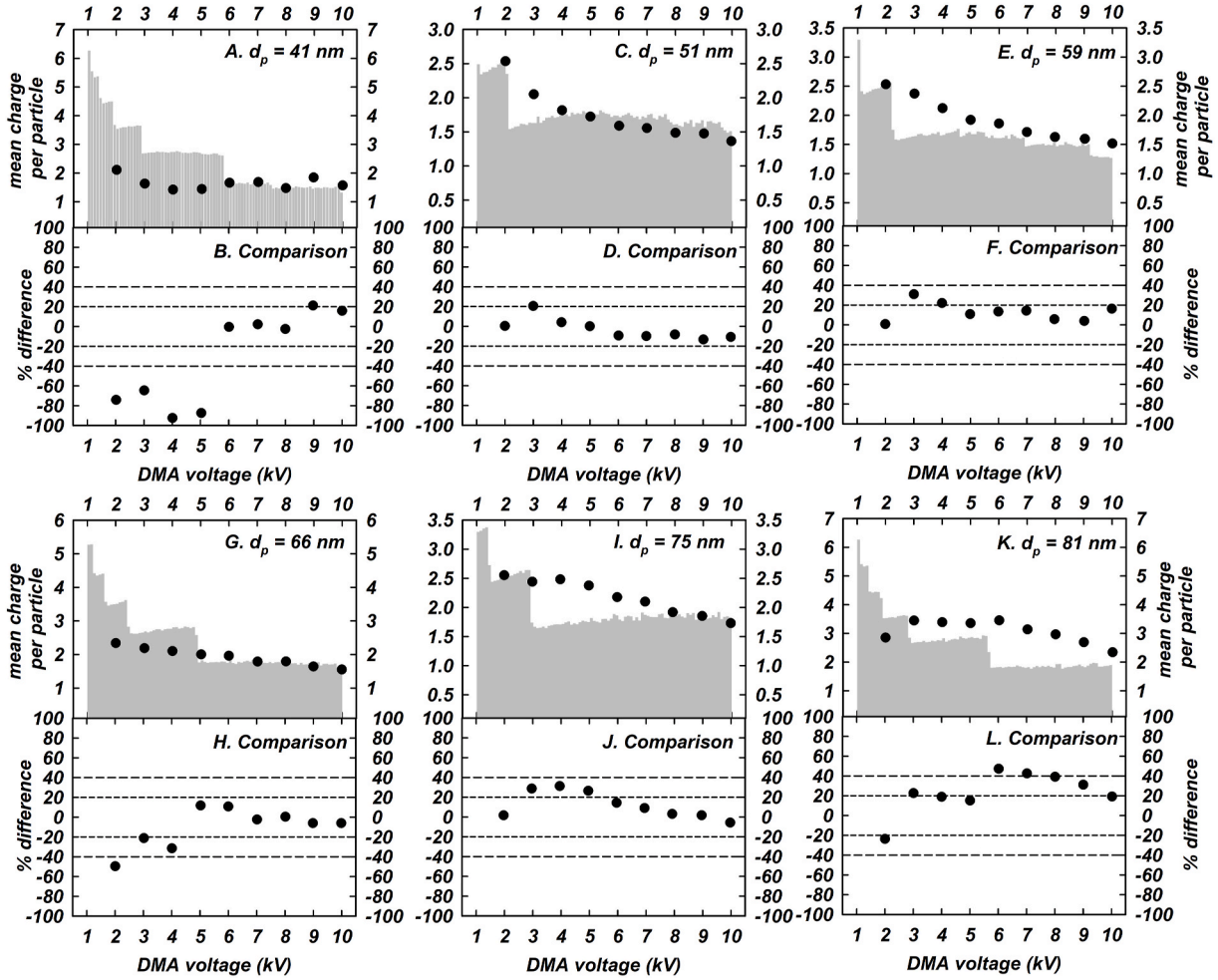


Fig. 13. Calculations of the bipolar charge distribution for experimental data reported by Wen et al. (1984) J. Aerosol Sci. 15 (2): 103–122 for iron oxide linear chain particles of primary particle diameter $d_p = 41 - 81$ nm in air. The ion properties used for model calculations using eq. (11) with the LD-based β_i (eq. (9) and eq. (10)) are tabulated in Sec. S3-F, SI. The steps for calculation of length scales R_s and PA from measured quantities for the linear chain (cylinder) charging data is described in Sec. S5, SI. The steps for calculation of particle mean charge p for comparison with the experimental data is described in Sec. S6, SI. p is plotted as a function of DMA classification voltage for A) $d_p = 41$ nm, C) $d_p = 51$ nm, E) $d_p = 59$ nm, G) $d_p = 66$ nm, I) $d_p = 75$ nm, K) $d_p = 81$ nm. The experimental data is shown using black filled circles and the model predictions are shown using the gray filled histogram. Panel B (" $d_p = 41$ nm"), panel D (" $d_p = 51$ nm"), panel F (" $d_p = 59$ nm"), panel H (" $d_p = 66$ nm"), panel J (" $d_p = 75$ nm"), panel L (" $d_p = 81$ nm") show the % difference, defined as $\left(1 - \frac{p^{exp}}{p^{calc}}\right)\%$, between experimental data and model predictions. Reference lines at $\pm 20\%$, $\pm 40\%$ are shown in panels B, D, F, H, J, L. In all model calculations, the particles are assumed to be conducting ($\epsilon_r \rightarrow \infty$).

shape on diffusion charging and deduce insights for the design of charging experiments using highly non-spherical particles. As illustrative examples, we choose four specific shapes: cylinders with $\frac{L_p}{d_p} = 100, 1000$ and fractal aggregates ($D_f = 1.3$, $k_f = 1.3$) that consist of N point contacting spheres with $N = 20, 100$ to illustrate the effect of particle shape on β_i and subsequently, the charge fractions f_p for $p = -2, -1, 0, +1, +2$. The non-spherical particle friction factor ζ_p is calculated based on the desired value of the electrical mobility equivalent diameter D_{me} , a common measure of size employed in electrical mobility analysis of non-spherical aerosol nanoparticles, at 1 atm, 300 K. The friction factor ζ_p of the cylinder/aggregate particle is iteratively calculated using the adjusted sphere model (Dahneke, 1973; Zhang et al., 2012) by suitably choosing the particle diameter d_p (for cylinders) or the primary particle diameter d_p (for aggregates) to vary the electrical mobility equivalent diameters in the range of 20–200 nm. The calculation of R_s , PA and the collision kernel β_i (using positive ions of mass $0.1 \frac{\text{kg}}{\text{mole}}$ and electrical mobility of $1.4 \times 10^{-4} \text{ m}^2 \text{ s}^{-1} \text{ V}^{-1}$ in eq. (9) and eq. (10)) for these shapes are carried out as per the steps laid out in Sec. S7, SI and used in eq. (11) for charge fraction f_p calculation. Fig. 14 presents computations of the ratio $\frac{\beta_i^{NS}}{\beta_i}$ for $D_{me} = 50, 80, 100, 200$ nm as a function of particle charge p (β_i^{NS} is the particle-ion

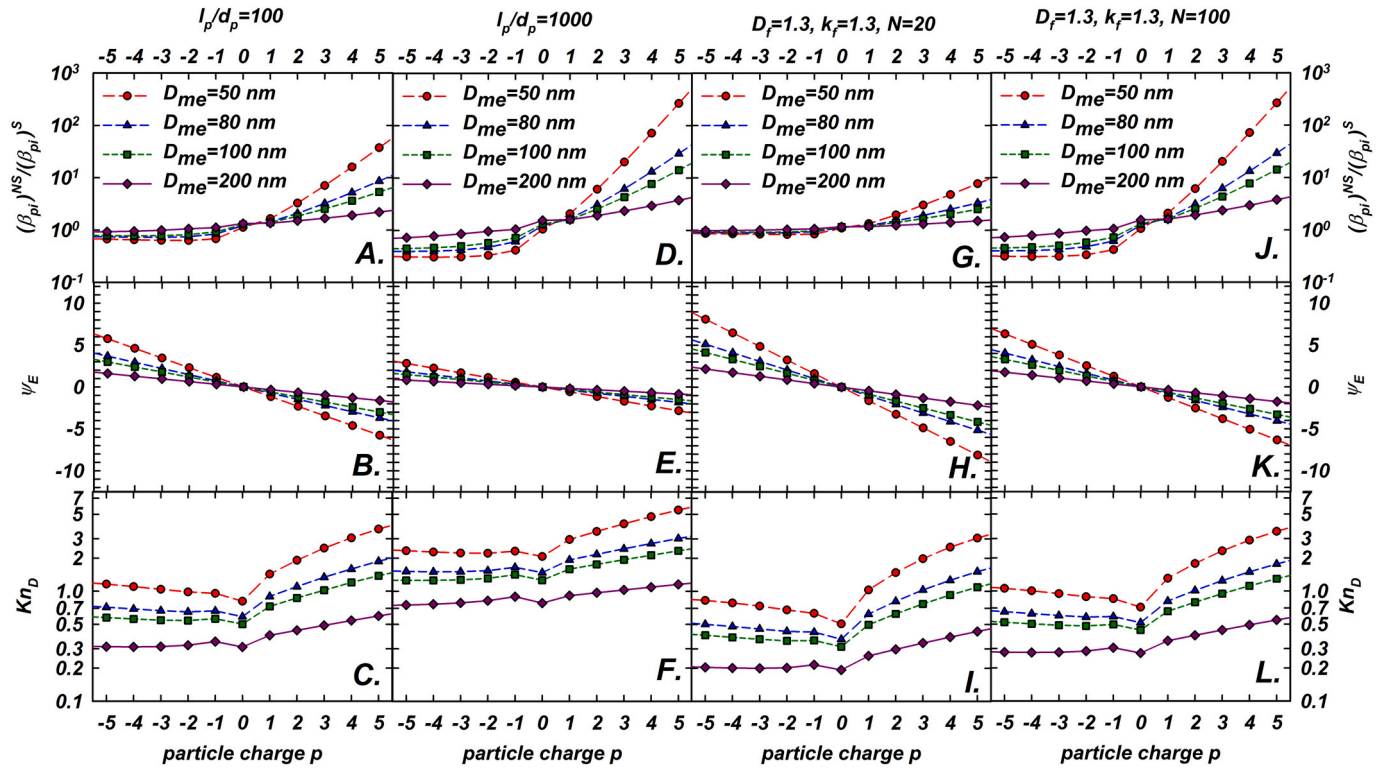


Fig. 14. Calculations of $\frac{(\beta_{pi})^{NS}}{(\beta_{pi})^S}$ for $D_{me} = 50, 80, 100, 200$ nm as a function of particle charge p in panels A, D, G, J, respectively. Also shown are ψ_E (panels B, E, H, K) and Kn_D (panel C, F, I, L) for charging conditions of 1 atm, 300 K and positive ion mass $0.1 \frac{\text{kg}}{\text{mole}}$ and electrical mobility of $1.4 \times 10^{-4} \text{ m}^2 \text{ s}^{-1} \text{ V}^{-1}$.

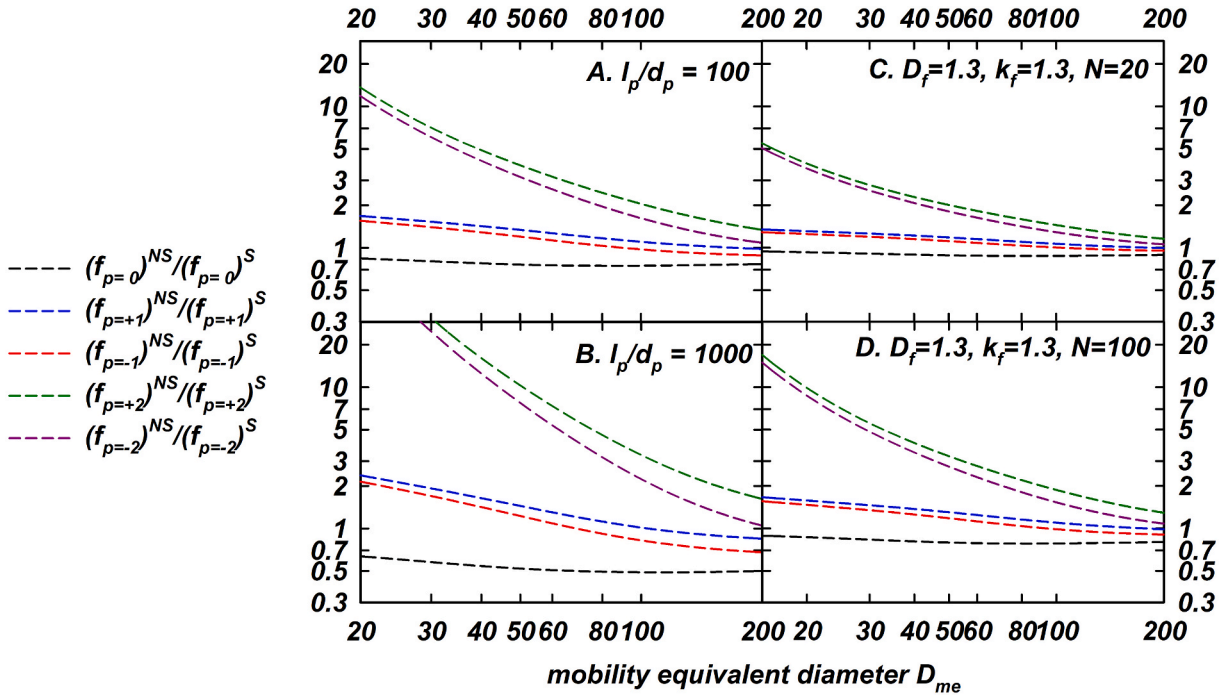


Fig. 15. Calculations of $\frac{f_p^{NS}}{f_p^S}$ as a function of D_{me} for $p = -2, -1, 0, +1, +2$ for particle shapes noted in the title of panels A–D.

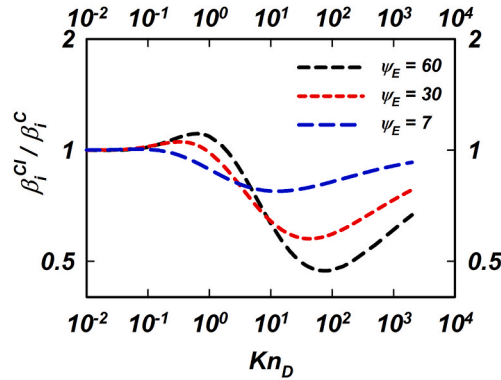


Fig. 16. Model calculations of the ratio $\frac{\beta_i^{CI}}{\beta_i^C}$ of the particle-ion collision kernel with and without image potential.

collision kernel for one of the four non-spherical particle shapes chosen and β_i^S is the corresponding value for the sphere with the same electrical mobility as the non-sphere). Also shown are ψ_E (panels B, E, H, K) and Kn_D (panel C, F, I, L) for the charging conditions chosen. For cylinders with $\frac{l_p}{d_p} = 100$ (panels A–C), it is seen that the effect of shape on β_i^{NS} is stronger for like charged particle-ion collisions ($p > 0$) than unlike charged particle-ion collisions ($p < 0$) and that the effect of shape diminishes with increasing mobility diameter. In past work on Coulombically driven collisions between unlike charged particle and an ion, a capture radius as a length scale of the collision process has been shown to applicable for spherical particles (Gatti & Kortshagen, 2008; Gopalakrishnan & Hogan, 2012). For non-spherical particles, a precise definition of such a capture radius is not known, at large particle-ion separations, the collisional volume is approximately spherical. Such a spherical symmetry is absent for like charged particle-ion potential interactions, possibly leading to a stronger dependence on shape. The same is true for cylinders with $\frac{l_p}{d_p} = 1000$, where the effect of shape is stronger: $\frac{\beta_i^{NS}}{\beta_i^S} \sim 10^2$ for $\frac{l_p}{d_p} = 100$ and $\frac{\beta_i^{NS}}{\beta_i^S} \sim 10^3$ for $\frac{l_p}{d_p} = 1000$. This translates into higher fraction of multiply charged particles as shown in Fig. 15 that presents charge distribution calculations (using positive and negative ions of mass $0.1 \frac{\text{kg}}{\text{mole}}$ and electrical mobility of $1.4 \times 10^{-4} \text{ m}^2 \text{ s}^{-1} \text{ V}^{-1}$, 300 K and 1 atm gas pressure) as ratio $\frac{f_p^{NS}}{f_p^S}$ as a function of D_{me} for $p = -2, -1, 0, +1, +2$, where f_p^{NS} is the fraction of particles carrying p charges from a population of non-spherical particles (NS) and f_p^S is the same for a population of spherical

particles (S) with the same electrical mobility as the non-spheres. Panel A of Fig. 15 shows that neutral and singly charged fractions are similar to that of spheres, higher order fractions ($p = \pm 2$) are significantly higher than spheres and are likely to lead to sensitive probing of the effect of particle shape. If the total concentration of aerosol particles generated and exposed to bipolar ions is high, the observation of charge states $p > 2$ may also be possible. This trend is further exacerbated for cylinders with $\frac{l_p}{d_p} = 1000$ (panel B of Fig. 15). For the case of fractal aggregates, panels G and J of Fig. 14 show that $\frac{\beta_i^{NS}}{\beta_i^S}$ follows a similar trend to that of cylinders and that shape significantly alters the collision kernel for repulsive Coulomb interactions. Consequently, strong deviation from the diffusion charging behavior of spherical particles is seen in panels C and D of Fig. 15, in which, like the case of cylinders, 5–10 times the fraction of $p = \pm 2$ particles are expected. Similar to the bipolar charge fraction measurements of Maricq (2008), measurement of triply or higher charge fractions for low fractal dimension aggregates (like the sample calculations for $D_f = 1.3$ here) will highlight the effect of particle shape on diffusion charging for the validation of models such as the one advanced here.

To illustrate the role of the image potential, we present a calculation of the ratio of the collision kernel between an arbitrary shaped particle and ion with image potential β_i^{CI} and without accounting for the image potential β_i^C for $\Psi_E = 60, 30, 7$ across the Kn_D range of 0.01 – 2000 in Fig. 16. As established previously, the β_i model for unlike charged particle-ion collisions (eq. (10)) is valid for arbitrary shapes and is used to understand the quantitative error introduced by neglecting the contribution of the image potential. It is seen that with increasing Ψ_E , the ratio $\frac{\beta_i^{CI}}{\beta_i^C} \sim 0.5$ for $10 < Kn_D < 1000$ indicating the importance of including the image potential for the charging of nm scale non-spherical particles. Also, $\frac{\beta_i^{CI}}{\beta_i^C} \rightarrow 1$ as $Kn_D \rightarrow 0$ indicating that in the continuum range the effect of image potential energy is countered by the ion's thermal energy. It is also evident that $\frac{\beta_i^{CI}}{\beta_i^C}$ may increase >1 for $Kn_D > 2000$ and that in the free molecular regime (low pressure and/or small particle sizes), the image potential is likely to have a significant effect on the collision kernel. The model developed for $0 < Kn_D \leq 2000$, that covers a wide range of particle size-pressure combinations, shows that the finite Kn_D transition regime charging is significantly influenced by the image potential. Finally, as $\Psi_E \rightarrow 0$, the effect of both Coulomb and image potential vanishes leading to purely hard-sphere interactions, as expected.

Lastly, a remark on the ion properties used for calculating charge fractions is in order. The use of a single value of ion mass and mobility has been frequently invoked in the past when detailed mass-mobility distributions were not available. In this article, we have used that approach for all the studies, except that of Gopalakrishnan et al. (2015) and Johnson et al. (2020) where ion-mass mobility distributions were available/estimated, for practical reasons and found reasonable agreement. Hence it is conceivable that the use of nominal properties may be adequate because the charge fraction predictions may be only weakly sensitive on the ion properties over a wide range (~ 50 – 1000 Da, 1 – 3×10^{-4} m²s⁻¹V⁻¹). Such nominal properties may be the mean, mode or other moments of a measured distribution and would need to be estimated based on a sensitivity analysis of the dependence of the charge fraction on the ion properties (i.e.) $\frac{\partial f_p}{\partial m_i}, \frac{\partial f_p}{\partial \mu_i}$. Such a sensitivity analysis for the charge fractions f_p may be easily carried out based on eq. (11) with eq. (9) and eq. (10) as input kernels. We refrain from presenting such an analysis and restrict our focus to diffusion charging collision kernel development and validation. The determination of optimal approximations for ion properties to give accurately predict experimentally measured charge fractions is beyond our scope here. Eq. (11) has been used in both cases wherein only approximate ion properties were known/estimated and cases where detailed mass-mobility data is available to make our charging collision kernel self-contained and straightforward to use.

4. Conclusions

In this article, we have used Langevin Dynamics (LD) simulations to calculate the collision kernel β_i for collisions between an unlike charged, conducting particle of arbitrary shape and an ion in the absence of external fields. The presented calculations of β_i for various test shapes allowed the extension of the particle-ion collision kernel β_i taking into account attractive Coulomb-potential interactions developed for spherical particles by Li et al. (2020) to particles of arbitrary shape. Along with this β_i model and the β_i model developed by Gopalakrishnan, Thajudeen, et al. (2013) for like charged collisions between ions and arbitrary shaped particles, complete bipolar charge distributions were computed and compared with experimental data from prior studies (Gopalakrishnan et al., 2015; Johnson et al., 2020; Maricq, 2008; Wen et al., 1984b; Wiedensohler & Fissan, 1991; Xiao et al., 2012). Based on the LD-based β_i model development and the comparison of charge distribution predictions with experimental data, we draw the following conclusions:

1. LD is a robust computational tool to calculate collision kernels or rate constants to describe mass transport of dilute species (ions in this instance) suspended in a background gas. The LD-computed collision kernel approaches the appropriate analytically derived continuum (high pressure and/or large particle, $Kn_D \rightarrow 0$) and free molecular (low pressure and/or small particle, $Kn_D \rightarrow \infty$) limits, and provides a viable approach for modeling transport processes in the mass transfer transition regime (intermediate Kn_D). The analysis of particle-ion collisions in this article assumed that the particle material is perfectly conducting. Differences between predictions and experimental data that arise from the assumption of particle material to be perfectly conducting ($\epsilon_r \rightarrow \infty$) require the accounting of the effect of particle material on β_i and needs to be investigated in future work. Also not considered in this study is the effect of external electric fields on the flux of ions transported onto the surface of a particle. The LD simulation approach is ideally suited to handle both of these effects.
2. The presented model (eq. (9) and eq. (10)) robustly describes the collision kernel β_i to describe the charging rate of arbitrary shape aerosol particles in the presence of attractive and repulsive Coulomb potential interactions while also accounting for the particle-ion

image potential as well. Thus, it represents a complete model to describe the bipolar and unipolar diffusion charging of non-spherical particles exposed to singly charged ions at a wide range of background gas temperature-pressure combinations may be described using the presented model for β_i in terms of H . The effect of shape is self-consistently captured through two length scales R_s, PA that can be calculated with knowledge of particle geometry alone.

3. The comparisons with bipolar charging data for spheres establish that the LD-based β_i model may be used to calculate particle charging in air, nitrogen and argon and is also accurate in predicting charge states up to ± 6 .
4. The comparisons with bipolar charging data for fractal aggregates show that for $D_f \geq 1.7$, the effect of shape is minimal and that particles behave similar to spheres of equivalent mobility. Calculations to probe the effect of particle shape, that show that for relatively low $D_f \sim 1.3$ aggregates are likely to show significant shape dependence, are presented to motivate future experimental studies that may be used for model validation.
5. The comparisons with bipolar charging data for linear chains and cylindrical particles shows excellent agreement over a wide range of $0.41 < \frac{PA}{\pi R_s^2} < 0.84$. Calculations that will aid the design of future experiments using very high aspect ratio cylindrical particles are also presented. These calculations suggest that higher order charge fractions ($|p| \geq 2$) are expected to be higher for highly non-spherical particles $\left(\frac{PA}{\pi R_s^2} \ll 1\right)$ compared to spheres of the same electrical mobility.
6. **Sec. S7, SI** describes the steps (represented schematically in Fig. S5, SI) to implement a calculation of the collision kernel for a non-spherical particle (aggregate/cylinder) of known shape parameters and ion properties for carrying out calculations of unipolar or bipolar diffusion charge distributions using eq. (11), that also allows taking into account the effect of ion polydispersity, wherever detailed ion mass-mobility distributions are available.

Online supplementary information (SI)

Animations of particle-ion collisions in the 1) continuum ($Kn_D \rightarrow 0$), 2) free molecular ($Kn_D \rightarrow \infty$) and 3) transition regimes (finite Kn_D) of diffusional ion motion.

Declaration of competing interest

The authors declare that they have no known competing financial interests or personal relationships that could have appeared to influence the work reported in this paper.

Acknowledgements

Funding for this work was provided by US National Science Foundation (NSF) PHY Grant Award Number 1903432 under the Directorate of Mathematical & Physical Sciences. We thank the University of Memphis High Performance Computing Cluster for providing computational resources to carry out this research.

SUPPLEMENTARY INFORMATION (SI)

Sec. S1: Continuum and free molecular enhancement factors for. $-60 \leq \Psi_E \leq 60$, $0 \leq \frac{\Psi_I}{|\Psi_E|} \leq 1$

Sec. S2: Regressions for $\mu(Kn_D, \Psi_E, \Psi_I)$ and $A(\Psi_E, \Psi_I)$, $B(\Psi_E, \Psi_I)$, $C(\Psi_E, \Psi_I)$, $k(\Psi_E, \Psi_I)$ and additional figs. S1 and S2.

Sec. S3: Ion properties used to compute theoretical charge distributions for comparison and additional figs. S3 and S4.

Sec. S4: Steps for calculation of length scales R_s and PA from measured quantities for the agglomerate charging data reported in Maricq (2008) and Xiao et al (2012).

Sec. S5: Steps for calculation of length scales R_s and PA from measured quantities for the cylinders charging data reported in Gopalakrishnan et al.

Sec. S6: Steps for calculation of particle mean charge p for comparison with the experimental data reported by Wen et al.

Sec. S7: Steps for calculating β_i from specified particle shape, size, ion properties and gas parameters and schematic fig. S5.

Appendix A. Supplementary data

Supplementary data to this article can be found online at <https://doi.org/10.1016/j.jaerosci.2020.105678>.

References

- Adachi, M., Kousaka, Y., & Okuyama, K. (1985). Unipolar and bipolar diffusion charging of ultrafine aerosol-particles. *Journal of Aerosol Science*, 16(2), 109–123.
- Adachi, M., Okuyama, K., Kousaka, Y., Kozuru, H., & Pui, D. Y. H. (1987). Diffusion charging of ultrafine aerosol-particles by positive helium, argon, and nitrogen-ions. *Journal of Applied Physics*, 62(7), 3050–3052. <https://doi.org/10.1063/1.339368>

- Adachi, M., Okuyama, K., Kousaka, Y., Kozuru, H., & Pui, D. Y. H. (1989). Bipolar diffusion charging of aerosol-particles under high particle ion concentration ratios. *Aerosol Science and Technology*, 11(2), 144–156. <https://doi.org/10.1080/02786828908959307>
- Adachi, M., Pui, D. Y. H., & Liu, B. Y. H. (1993). Aerosol charge neutralization by a corona ionizer. *Aerosol Science and Technology*, 18(1), 48–58. <https://doi.org/10.1080/02786829308959583>
- Adachi, M., Romay, F. J., & Pui, D. Y. H. (1992). High-efficiency unipolar aerosol charger using a radioactive alpha-source. *Journal of Aerosol Science*, 23(2), 123–137. [https://doi.org/10.1016/0021-8502\(92\)90049-2](https://doi.org/10.1016/0021-8502(92)90049-2)
- Allen, J. E. (1992). Probe theory - the orbital motion approach. [Article; Proceedings Paper]. *Physica Scripta*, 45(5), 497–503. <https://doi.org/10.1088/0031-8949/45/5/013>
- Biskos, G., Mastorakos, E., & Collings, N. (2004). Monte-carlo simulation of unipolar diffusion charging for spherical and non-spherical particles. *Journal of Aerosol Science*, 35(6), 707–730. <https://doi.org/10.1016/j.jaerosci.2003.11.010>
- Biskos, G., Reavell, K., & Collings, N. (2005). Unipolar diffusion charging of aerosol particles in the transition regime. *Journal of Aerosol Science*, 36(2), 247–265. <https://doi.org/10.1016/j.jaerosci.2004.09.002>
- Boisdron, Y., & Brock, J. R. (1970). On the stochastic nature of the acquisition of electrical charge and radioactivity by aerosol particles. *Atmospheric Environment*, 4(1), 35–50. [https://doi.org/10.1016/0004-6981\(70\)90052-1](https://doi.org/10.1016/0004-6981(70)90052-1), 1967.
- Bricard, J. (1962). La fixation des petits ions atmosphériques sur les aérosols ultra-fins. *Geofisica pura e applicata*, 51(1), 237–242. <https://doi.org/10.1007/BF01992666>
- Brown, R. C., & Hemingway, M. A. (1995). Electric charge distribution and capacitance of agglomerates of spherical particles: Theory and experimental simulation. *Journal of Aerosol Science*, 26(8), 1197–1206. [https://doi.org/10.1016/0021-8502\(95\)00524-2](https://doi.org/10.1016/0021-8502(95)00524-2)
- Carsi, M., & Alonso, M. (2020). A numerical study of bipolar charging and neutralization of ultrafine particles with uniformly generated heterogeneous ions. *Journal of Aerosol Science*, 149, 105611. <https://doi.org/10.1016/j.jaerosci.2020.105611>
- Chahl, H. S., & Gopalakrishnan, R. (2019). High potential, near free molecular regime coulombic collisions in aerosols and dusty plasmas. *Aerosol Science and Technology*, 53(8), 933–957. <https://doi.org/10.1080/02786826.2019.1614522>
- Chang, J. S. (1981). Theory of diffusion charging of arbitrarily shaped conductive aerosol-particles by unipolar ions. *Journal of Aerosol Science*, 12(1), 19–26. [https://doi.org/10.1016/0021-8502\(81\)90006-9](https://doi.org/10.1016/0021-8502(81)90006-9)
- Chang, J. S., & Laframboise, J. G. (1976). Probe theory for arbitrary shape in a large debye length, stationary plasma. *The Physics of Fluids*, 19(1), 25–31. <https://doi.org/10.1063/1.861324>
- D'Yachkov, L. G., Khrapak, A. G., Khrapak, S. A., & Morfill, G. (2007). Model of grain charging in collisional plasmas accounting for collisionless layer. *Physics of Plasmas*, 14.
- Dahneke, B. E. (1973). Slip correction factors for nonspherical bodies- iii the form of the general law. *Journal of Aerosol Science*, 4, 163–170.
- Davison, S. W., Yu, P. Y., Hwang, S. Y., & Gentry, J. W. (1986). Experimental measurements of the rate of unipolar charging for spherical and nonspherical particles. *Journal of Aerosol Science*, 17(3), 481–483. [https://doi.org/10.1016/0021-8502\(86\)90139-4](https://doi.org/10.1016/0021-8502(86)90139-4)
- Filippov, A. V. (1994). Charge-distribution among nonspherical particles in a bipolar ion environment. *Journal of Aerosol Science*, 25(4), 611–615. [https://doi.org/10.1016/0021-8502\(94\)90002-7](https://doi.org/10.1016/0021-8502(94)90002-7)
- Friedlander, S. K. (2000). *Smoke, dust, and haze: Fundamentals of aerosol dynamics*, null.
- Fuchs, N. A. (1963). On the stationary charge distribution on aerosol particles in a bipolar ionic atmosphere. *Geofisica Pura e Applicata*, 51, 185–193.
- Gatti, M., & Kortschagen, U. (2008). Analytical model of particle charging in plasmas over a wide range of collisionality. *Physical Review E*, 78(4), Article 046402. <https://doi.org/10.1103/PhysRevE.78.046402>
- Gopalakrishnan, R., & Hogan, C. J. (2011). Determination of the transition regime collision kernel from mean first passage times. *Aerosol Science and Technology*, 45(12), 1499–1509. <https://doi.org/10.1080/02786826.2011.601775>
- Gopalakrishnan, R., & Hogan, C. J. (2012). Coulomb-influenced collisions in aerosols and dusty plasmas. *Physical Review E*, 85, Article 026410.
- Gopalakrishnan, R., McMurry, P. H., & Hogan, C. J. (2015). The bipolar diffusion charging of nanoparticles: A review and development of approaches for non-spherical particles. *Aerosol Science and Technology*, 49(12), 1181–1194. <https://doi.org/10.1080/02786826.2015.1109053>
- Gopalakrishnan, R., Meredith, M. J., Larriba-Andaluz, C., & Hogan, C. J. (2013). Brownian dynamics determination of the bipolar steady state charge distribution on spheres and non-spheres in the transition regime. *Journal of Aerosol Science*, 63, 126–145. <https://doi.org/10.1016/j.jaerosci.2013.04.007>
- Gopalakrishnan, R., Thajudeen, T., & Hogan, C. J., Jr. (2011). Collision limited reaction rates for arbitrarily shaped particles across the entire diffusive knudsen number range. *The Journal of Chemical Physics*, 135(5), Article 054302. <https://doi.org/10.1063/1.3617251>
- Gopalakrishnan, R., Thajudeen, T., Ouyang, H., & Hogan, C. J. (2013). The unipolar diffusion charging of arbitrary shaped aerosol particles. *Journal of Aerosol Science*, 64, 60–80. <https://doi.org/10.1016/j.jaerosci.2013.06.002>, 0.
- Han, R. J., & Gentry, J. W. (1993). Unipolar diffusional charging of fibrous aerosols—theory and experiment. *Journal of Aerosol Science*, 24(2), 211–226. [https://doi.org/10.1016/0021-8502\(93\)90059-1](https://doi.org/10.1016/0021-8502(93)90059-1)
- Han, R. J., & Gentry, J. W. (1994). Evolution of charge-distributions of nonspherical particles undergoing unipolar charging. *Journal of Aerosol Science*, 25(3), 499–508. [https://doi.org/10.1016/0021-8502\(94\)90067-1](https://doi.org/10.1016/0021-8502(94)90067-1)
- Han, R. J., Ranade, M. B., & Gentry, J. W. (1991a). Experimental-measurement of unipolar charging of carbon-fibers. *Journal of Aerosol Science*, 22, S231–S234. [https://doi.org/10.1016/s0021-8502\(05\)80077-1](https://doi.org/10.1016/s0021-8502(05)80077-1)
- Han, R. J., Ranade, M. B., & Gentry, J. W. (1991b). Rate of unipolar charging of ultrafine thin platelets. *Aerosol Science and Technology*, 15(3), 184–190. <https://doi.org/10.1080/02786829108959525>
- Hansen, S. (2004). Translational friction coefficients for cylinders of arbitrary axial ratios estimated by Monte Carlo simulation. [Article]. *The Journal of Chemical Physics*, 121(18), 9111–9115. <https://doi.org/10.1063/1.1803533>
- Hoppel, W. A., & Frick, G. M. (1986). Ion-aerosol attachment coefficients and the steady-state charge distribution on aerosols in a bipolar ion environment. *Aerosol Science and Technology*, 5(1), 1–21.
- Hussin, A., Scheibel, H. G., Becker, K. H., & Porstendörfer, J. (1983). Bipolar diffusion charging of aerosol particles—I: Experimental results within the diameter range 4–30 nm. *Journal of Aerosol Science*, 14(5), 671–677.
- Jackson, J. D. (1975). *Classical electrodynamics*. New York: John Wiley and Sons.
- Johnson, T. J., Nishida, R. T., Irwin, M., Symonds, J. P. R., Olfert, J. S., & Boies, A. M. (2020). Measuring the bipolar charge distribution of nanoparticles: Review of methodologies and development using the aerodynamic aerosol classifier. *Journal of Aerosol Science*, 143, 105526. <https://doi.org/10.1016/j.jaerosci.2020.105526>
- Kim, I. C., & Torquato, S. (1991). 1st-passage-time calculation of the conductivity of continuum models of multiphase composites. *Physical Review A*, 43(6), 3198–3201.
- Knutson, E. O., & Whitby, K. T. (1975). Aerosol classification by electric mobility: Apparatus, theory, and applications. *Journal of Aerosol Science*, 6(6), 443–451. [https://doi.org/10.1016/0021-8502\(75\)90060-9](https://doi.org/10.1016/0021-8502(75)90060-9)
- Ku, B. K., Deye, G. J., Kulkarni, P., & Baron, P. A. (2011). Bipolar diffusion charging of high-aspect ratio aerosols. *Journal of Electrostatics*, 69(6), 641–647. <https://doi.org/10.1016/j.elstat.2011.08.006>
- Kulkarni, P., Deye, G. J., & Baron, P. A. (2009). Bipolar diffusion charging characteristics of single-wall carbon nanotube aerosol particles. *Journal of Aerosol Science*, 40(2), 164–179. <https://doi.org/10.1016/j.jaerosci.2008.09.008>
- Laframboise, J. G., & Chang, J.-S. (1977). Theory of charge deposition on charged aerosol particles of arbitrary shape. *Journal of Aerosol Science*, 8(5), 331–338. [https://doi.org/10.1016/0021-8502\(77\)90020-9](https://doi.org/10.1016/0021-8502(77)90020-9)
- Leppä, J., Mui, W., Grantz, A. M., & Flagan, R. C. (2017). Charge distribution uncertainty in differential mobility analysis of aerosols. *Aerosol Science and Technology*, 51(10), 1168–1189. <https://doi.org/10.1080/02786826.2017.1341039>

- Li, L., Chahl, H. S., & Gopalakrishnan, R. (2020). Comparison of the predictions of Langevin dynamics-based diffusion charging collision kernel models with canonical experiments. *Journal of Aerosol Science*, 140, 105481. <https://doi.org/10.1016/j.jaerosci.2019.105481>
- Liu, Y., Attoui, M., Yang, K., Chen, J., Li, Q., & Wang, L. (2020). Size-resolved chemical composition analysis of ions produced by a commercial soft x-ray aerosol neutralizer. *Journal of Aerosol Science*, 147, 105586. <https://doi.org/10.1016/j.jaerosci.2020.105586>
- Lopez-Yglesias, X., & Flagan, R. C. (2013). Ion-aerosol flux coefficients and the steady-state charge distribution of aerosols in a bipolar ion environment. *Aerosol Science and Technology*, 47(6), 688–704. <https://doi.org/10.1080/02786826.2013.783684>
- Lushnikov, A. A., & Kulmala, M. (2004). Flux-matching theory of particle charging. *Physical Review E*, 70(4), Article 046413.
- Maißer, A., Thomas, J. M., Larriba-Andaluz, C., He, S., & Hogan, C. J. (2015). The mass-mobility distributions of ions produced by a po-210 source in air. *Journal of Aerosol Science*, 90, 36–50. <https://doi.org/10.1016/j.jaerosci.2015.08.004>
- Maricq, M. M. (2008). Bipolar diffusion charging of soot aggregates. *Aerosol Science and Technology*, 42(4), 247–254. <https://doi.org/10.1080/02786820801958775>
- Marlow, W. H. (1980). Derivation of aerosol collision rates for singular attractive contact potentials. *The Journal of Chemical Physics*, 73(12), 6284–6287. <https://doi.org/10.1063/1.440126>
- Mohnen, V. A. (1974). Formation, nature, and mobility of ions of atmospheric importance. In H. Dolezalek, & R. Reiter (Eds.), *Electrical processes in atmospheres - proceedings of the fifth international conference on atmospheric electricity held at garmisch-partenkirchen (Germany), 2–7 september 1974*. Steinkopff-Verlag Heidelberg.
- Mott-Smith, H. M., & Langmuir, I. (1926). The theory of collectors in gaseous discharges. *Physical Review*, 28(4), 727–763.
- Nie, Y., Wang, Y., & Biswas, P. (2017). Mobility and bipolar diffusion charging characteristics of crumpled reduced graphene oxide nanoparticles synthesized in a furnace aerosol reactor. *Journal of Physical Chemistry C*, 121(19), 10529–10537. <https://doi.org/10.1021/acs.jpcc.7b00189>
- Northrup, S. H., Allison, S. A., & McCammon, J. A. (1984). Brownian dynamics simulation of diffusion-influenced bimolecular reactions. *The Journal of Chemical Physics*, 80(4), 1517–1526.
- Oh, H., Park, H., & Kim, S. (2004). Effects of particle shape on the unipolar diffusion charging of nonspherical particles. *Aerosol Science and Technology*, 38(11), 1045–1053. <https://doi.org/10.1080/027868290883324>
- Ouyang, H., Gopalakrishnan, R., & Hogan, C. J., Jr. (2012). Nanoparticle collisions in the gas phase in the presence of singular contact potentials. *The Journal of Chemical Physics*, 137(6), Article 064316. <https://doi.org/10.1063/1.4742064>
- Park, M., Park, K., Moon, H. J., Ko, S. H., & Shin, W. G. (2015). The effect of particle morphology on unipolar diffusion charging of silver nanowires. *Aerosol Science and Technology*, 49(5), 290–298. <https://doi.org/10.1080/02786826.2015.1024305>
- Pease, L. F., Tsai, D. H., Brorson, K. A., Guha, S., Zachariah, M. R., & Tarlov, M. J. (2011). Physical characterization of icosahedral virus ultra structure, stability, and integrity using electrospray differential mobility analysis. [Article]. *Analytical Chemistry*, 83(5), 1753–1759. <https://doi.org/10.1021/ac1030094>
- Pease, L. F., Tsai, D. H., Hertz, J. L., Zangmeister, R. A., Zachariah, M. R., & Tarlov, M. J. (2010). Packing and size determination of colloidal nanoclusters. [Article]. *Langmuir*, 26(13), 11384–11390. <https://doi.org/10.1021/la100839t>
- Porstendorfer, J., Hussin, A., Scheibel, H. G., & Becker, K. H. (1984). Bipolar diffusion charging of aerosol-particles .2. Influence of the concentration ratio of positive and negative-ions on the charge distribution. [Article]. *Journal of Aerosol Science*, 15(1), 47. [https://doi.org/10.1016/0021-8502\(84\)90055-7](https://doi.org/10.1016/0021-8502(84)90055-7)
- Porstendorfer, J., Robig, G., & Ahmed, A. (1979). Experimental determination of the attachment coefficients of atoms and ions on monodisperse aerosols. [Article]. *Journal of Aerosol Science*, 10(1), 21–28.
- Potter, M. J., Luty, B., Zhou, H. X., & McCammon, J. A. (1996). Time-dependent rate coefficients from brownian dynamics simulations. *Journal of Physical Chemistry*, 100(12), 5149–5154.
- Reischl, G. P., Scheibel, H. G., & Porstendorfer, J. (1983). The bipolar charging of aerosols: Experimental results in the size range below 20-nm particle diameter. *Journal of Colloid and Interface Science*, 91(1), 272–275. [https://doi.org/10.1016/0021-9797\(83\)90332-6](https://doi.org/10.1016/0021-9797(83)90332-6)
- Rogak, S. N., & Flagan, R. C. (1992). Bipolar diffusion charging of spheres and agglomerate aerosol-particles. *Journal of Aerosol Science*, 23(7), 693–710. [https://doi.org/10.1016/0021-8502\(92\)90037-v](https://doi.org/10.1016/0021-8502(92)90037-v)
- Rubinstein, J., & Torquato, S. (1988). Diffusion-controlled reactions - mathematical formulation, variational-principles, and rigorous bounds. *The Journal of Chemical Physics*, 88(10), 6372–6380.
- Sharma, G., Wang, Y., Chakrabarty, R., & Biswas, P. (2019). Modeling simultaneous coagulation and charging of nanoparticles at high temperatures using the method of moments. *Journal of Aerosol Science*, 132, 70–82. <https://doi.org/10.1016/j.jaerosci.2019.03.011>
- Shin, W. G., Wang, J., Mertler, M., Sachweh, B., Fissan, H., & Pui, D. Y. H. (2010). The effect of particle morphology on unipolar diffusion charging of nanoparticle agglomerates in the transition regime. *Journal of Aerosol Science*, 41(11), 975–986. <https://doi.org/10.1016/j.jaerosci.2010.07.004>
- Shvartsburg, A. A., Mashkevich, S. V., Baker, E. S., & Smith, R. D. (2007). Optimization of algorithms for ion mobility calculations. *The Journal of Physical Chemistry A*, 111(10), 2002–2010.
- Stolzenburg, M. R., & McMurry, P. H. (2008). Equations governing single and tandem dma configurations and a new lognormal approximation to the transfer function. *Aerosol Science and Technology*, 42(6), 421–432. <https://doi.org/10.1080/02786820802157823>
- Tanaka, Y., Higashi, H., Manirakiza, E., Seto, T., Otani, Y., & Hirasawa, M. (2014). Charge neutralization of aerosol carbon nanofibers. *Journal of Chemical Engineering of Japan*, 47(8), 644–650. <https://doi.org/10.1252/jcej.14we010>
- Thajudeen, T., Gopalakrishnan, R., & Hogan, C. J. (2012). The collision rate of non-spherical particles and aggregates for all diffusive knudsen numbers. *Aerosol Science and Technology*, 46(11).
- Torquato, S., & Avellaneda, M. (1991). Diffusion and reaction in heterogeneous media - pore-size distribution, relaxation-times, and mean survival-time. *The Journal of Chemical Physics*, 95(9), 6477–6489.
- Unger, L., Boulaud, D., & Borra, J. P. (2004). Unipolar field charging of particles by electrical discharge: Effect of particle shape. *Journal of Aerosol Science*, 35(8), 965–979. <https://doi.org/10.1016/j.jaerosci.2004.01.006>
- Vincenti, W. G., & Kruger, C. H. (1975). *Introduction to physical gas dynamics*. Huntington, NY: Krieger.
- Vohra, K. G., Subbaramu, M. C., & Vaseduvam, K. N. (1969). *Nucleation of water cluster ions*. Bombay: Bhabha Atomic Research Center.
- Vomela, R. A., & Whitby, K. T. (1967). The charging and mobility of chain aggregate smoke particles. *Journal of Colloid and Interface Science*, 25(4), 568–576. [https://doi.org/10.1016/0021-9797\(67\)90070-7](https://doi.org/10.1016/0021-9797(67)90070-7)
- Wen, H. Y., Reischl, G. P., & Kasper, G. (1984a). Bipolar diffusion charging of fibrous aerosol-particles .1. Charging theory. *Journal of Aerosol Science*, 15(2), 89–101. [https://doi.org/10.1016/0021-8502\(84\)90029-6](https://doi.org/10.1016/0021-8502(84)90029-6)
- Wen, H. Y., Reischl, G. P., & Kasper, G. (1984b). Bipolar diffusion charging of fibrous aerosol-particles .2. Charge and electrical mobility measurements on linear-chain aggregates. *Journal of Aerosol Science*, 15(2), 103–122. [https://doi.org/10.1016/0021-8502\(84\)90030-2](https://doi.org/10.1016/0021-8502(84)90030-2)
- Wiedensohler, A., & Fissan, H. J. (1991). Bipolar charge-distributions of aerosol-particles in high-purity argon and nitrogen. *Aerosol Science and Technology*, 14(3), 358–364. <https://doi.org/10.1080/02786829108959498>
- Xiao, K., Swanson, J. J., Pui, D. Y. H., & Kittelson, D. B. (2012). Bipolar diffusion charging of aggregates. *Aerosol Science and Technology*, 46(7), 794–803. <https://doi.org/10.1080/02786826.2012.667585>
- Yu, P. Y., Wang, C. C., & Gentry, J. W. (1987). Experimental-measurement of the rate of unipolar charging of actinolite fibers. *Journal of Aerosol Science*, 18(1), 73–85. [https://doi.org/10.1016/0021-8502\(87\)90012-7](https://doi.org/10.1016/0021-8502(87)90012-7)
- Zhang, C., Thajudeen, T., Larriba, C., Schwartzentruber, T. E., & Hogan, C. J. (2012). Determination of the scalar friction factor for nonspherical particles and aggregates across the entire knudsen number range by direct simulation Monte Carlo (dsmc). *Aerosol Science and Technology*, 46(10), 1065–1078. <https://doi.org/10.1080/02786826.2012.690543>
- Zhou, H. X. (1995). Calculation of translational friction and intrinsic viscosity .1. General formulation for arbitrarily shaped particles. [Article]. *Biophysical Journal*, 69(6), 2286–2297.
- Zhou, H. X., Szabo, A., Douglas, J. F., & Hubbard, J. B. (1994). A brownian dynamics algorithm for calculating the hydrodynamic friction and the electrostatic capacitance of an arbitrarily-shaped object. *The Journal of Chemical Physics*, 100(5), 3821–3826.